

Probing sub-GeV leptophilic dark matter at Belle II and NA64

Jinhan Liang,^a Zuowei Liu^{a,b} and Lan Yang^a

^a*Department of Physics, Nanjing University,
Nanjing 210093, China*

^b*CAS Center for Excellence in Particle Physics,
Beijing 100049, China*

E-mail: jinhanliang@smail.nju.edu.cn, zuoweiliu@nju.edu.cn,
lanyang@smail.nju.edu.cn

ABSTRACT:

An analysis is given of the Belle II sensitivities and NA64 constraints on the sub-GeV Dirac dark matter that interacts with charged leptons. We consider two different types of interactions between sub-GeV Dirac dark matter and the charged leptons: the EFT operators and the light vector mediators. We compute the Belle II mono-photon sensitivities on sub-GeV dark matter with 50 ab^{-1} data which are expected to be accumulated in the full Belle II runs. Although the Belle II mono-photon sensitivities on the EFT operators are of similar size as the LEP constraints, Belle II can probe new parameter space of the light vector mediator models that are unexplored by LEP. For both the EFT operators and the light vector mediator models, the Belle II mono-photon sensitivities can be several orders of magnitude stronger than the current dark matter direct detection limits, as well as the white dwarf limits. The light vector mediator can also be directly searched for by reconstructing the invariant mass of its di-lepton decay final states at Belle II, which is found to be complementary to the mono-photon channel. We compute the NA64 constraints on the sub-GeV Dirac dark matter and provide analytic expressions of the dark matter cross section in the Weizsäcker-Williams approximation, for the EFT operators, and for the light vector mediator models. We find that the current NA64 data (with 2.84×10^{11} electron-on-target events) provide strong constraints on sub-GeV dark matter. Although the NA64 constraints are found to be about one order of magnitude smaller than the Belle II sensitivities for the EFT operators, NA64 can probe some regions of the parameter space in the light vector mediator models that are beyond the reach of Belle II. We also find that Belle II and NA64 can probe the canonical dark matter annihilation cross section in thermal freeze-out in a significant portion of the parameter space of the models considered.

KEYWORDS: Beyond Standard Model, Effective Field Theory, Gauge Theory, Belle II, NA64, sub-GeV DM

ARXIV EPRINT: [2111.15533](https://arxiv.org/abs/2111.15533)

Contents

1	Introduction	1
2	Dark Matter Models and the mono-photon signal	3
3	Mono-photon searches at Belle II	4
4	Mono-photon constraints on EFT operators	5
5	Mono-photon constraints on light mediator model	7
6	Di-lepton constraints on light mediator models	11
7	NA64 constraints	14
8	Dark matter relic density	18
9	Summary	19
10	Acknowledgement	20
A	DM production cross sections at NA64	20
B	Mono-photon cross sections of the EFT operators at Belle II	22
C	Matrix elements for EFT operators in DMDD	23
D	LEP analysis	24
E	Confidence Level Limits	25
F	DM annihilation cross sections	26

1 Introduction

Although dark matter (DM) makes up a quarter of the total energy density of the universe, its particle property remains unknown today [1, 2]. During the past decades, a great amount of theoretical and experimental efforts have been put into searches for the weakly interacting massive particles (WIMPs), which have constrained the DM-nucleus cross section to an unprecedented level [3, 4]. Recently, dark matter direct detection (DMDD) experiments have also started to provide compelling limits on sub-GeV dark matter particles. For sub-GeV dark matter, electronic signals become important in DMDD experiments. Scattered by

DM, electrons in the target can be either ionized or excited. The DMDD experiments with an ionization signal include XENON10 [5], XENON100 [5], XENON1T [6], DarkSide-50 [7], and PandaX [8]; the experiments with an excitation signal include SENSEI [9], DAMIC [10], EDELWEISS [11], and SuperCDMS [12]. The excitation signal can have a lower energy threshold than the ionization signal, leading to a better sensitivity for lighter dark matter. Currently, the xenon target experiments and SENSEI provide the leading DMDD constraints to sub-GeV DM. Astrophysical processes can also give competitive constraints to sub-GeV DM, for example, heating constraints in white dwarfs due to DM [13–18]. Furthermore, interactions between sub-GeV DM and cosmic rays [19–21], and Sun [22, 23] can significantly alter the velocity of the DM particle, and thus enhance the sensitivity of the DMDD experiments.

In this paper, we study the Belle II sensitivities and the NA64 constraints on the sub-GeV dark matter that interacts with charged leptons. Belle II is operated at SuperKEKB which collides 7 GeV electrons with 4 GeV positrons [24]. In the 8-year data taking, Belle II is expected to accumulate 50 ab^{-1} data [24], which is much more than other low energy electron-positron colliders, such as BaBar and BESIII. Moreover, the calorimeter of Belle II is much more hermetic with non-projective barrel crystals, which makes it an ideal detector for DM searches [24, 25].

Electron collider constraints on DM have been studied previously, including Belle II [24, 26–31, 31–34], LEP [35–39], and other electron colliders [40–60]. In this paper, we study the capability of the Belle II experiment in probing the parameter space of the sub-GeV dark matter models, including both the effective field theory (EFT) operators and the light vector mediator models. To our knowledge, Belle II constraints on various EFT operators between DM and charged leptons have not been thoroughly studied in the literature. Certain light mediator models, e.g., the dark photon model has been studied in Ref. [24]. Here we consider a more general light mediator model in which the light mediator has both vector and axial-vector couplings to fermions in the hidden sector and in the SM sector. Thus we carry out detailed Belle II analyses both for the EFT operators and for the light mediator models with different mass relations and different couplings. We compute the mono-photon constraints on the EFT operators and on the light mediator models, and further compare the limits to the DMDD constraints. We find that the Belle II mono-photon limits can be much stronger than current DMDD constraints, and can also constrain the proposed DM models to interpret the recent excess events in Xenon1T electron recoil data [61]. For the light mediator models, we further compute the Belle II limits due to the visible decay final states of the mediator, and find that the visible channel can be complementary to the mono-photon channel.

NA64 is an electron fixed target experiment operated at CERN with the incident electron energy of $\sim 100 \text{ GeV}$ and a lead target. NA64 has collected 2.84×10^{11} electron-on-target (EOT) data in the year 2016, 2017, and 2018 [62]. The DM signature at NA64 is a significant missing energy [62]. NA64 constraints on DM have been analyzed recently, including DM with a dark photon mediator [62, 63], millicharged DM [64], DM with EM form factors [65], and pseudo-Dirac dark matter [66].

In this work, we carry out a systematic study on NA64 constraints for a number of DM

models (EFT operators and the light vector mediator models), which, to our knowledge, has not been done in the literature. We also provide analytic expressions of the differential cross sections for various models in the Weizsäcker-Williams approximation (WWA) [67, 68]. We find that NA64 and Belle II can be complementary in probing sub-GeV DM models.

The rest of the paper is organized as follows. In Sec. 2, we introduce two different types of dark matter models: fermionic DM interacting with SM via EFT operators and via the light vector mediator models. We discuss both the signal events and the SM background events in the mono-photon channel for the Belle II analysis in Sec. 3. We compute the Belle II mono-photon sensitivities for the EFT operators and for the light vector mediator models in Sec. 4 and Sec. 5 respectively, and further compare them to the DMDD limits. We analyze the Belle II di-muon limits on the light vector mediator models in Sec. 6. We compute the NA64 constraints on the EFT operators and on the light vector mediator models in Sec. 7. The analytic expressions of the DM cross sections in the WWA at the NA64 experiment are given in Appendix A. We compute the Belle II sensitivities on the dark matter annihilation cross section in Sec. 8. We summarize our findings in Sec. 9.

2 Dark Matter Models and the mono-photon signal

In this paper, we consider two different types of DM models: (1) fermionic DM interacts with charged leptons via EFT operators; (2) fermionic DM interacts with charged leptons via a light vector mediator. There are a variety of EFT operators between the SM and dark matter. Here we consider the fermionic dark matter that has four-fermion EFT interaction with charged leptons as follows [39, 46]

$$\mathcal{L} = \frac{1}{\Lambda_V^2} O_V \equiv \frac{1}{\Lambda_V^2} \bar{\chi} \gamma_\mu \chi \bar{\ell} \gamma^\mu \ell, \quad (2.1)$$

$$\mathcal{L} = \frac{1}{\Lambda_A^2} O_A \equiv \frac{1}{\Lambda_A^2} \bar{\chi} \gamma_\mu \gamma_5 \chi \bar{\ell} \gamma^\mu \gamma_5 \ell, \quad (2.2)$$

$$\mathcal{L} = \frac{1}{\Lambda_s^2} O_s \equiv \frac{1}{\Lambda_s^2} \bar{\chi} \chi \bar{\ell} \ell, \quad (2.3)$$

$$\mathcal{L} = \frac{1}{\Lambda_t^2} O_t \equiv \frac{1}{\Lambda_t^2} \bar{\chi} \ell \bar{\ell} \chi, \quad (2.4)$$

where χ is the Dirac DM, ℓ is the SM charged lepton, and Λ is the new physics scale. The first three EFT operators can be obtained by integrating out an s -channel mediator in a UV complete model; the last EFT operator can be obtained by integrating out a t -channel mediator [39]. Thus, we use Λ_V (Λ_A) to denote the vector (axial-vector) case; for the two scalar operators we use Λ_s and Λ_t to refer to the possible UV-completions.¹ The production cross section of $e^+e^- \rightarrow \bar{\chi}\chi\gamma$ at electron colliders for the above four EFT operators are computed in Ref. [46]; we collect these cross section formulas in Appendix B.

We consider a light mediator model in which the light mediator is a spin one particle with couplings to both hidden sector dark matter and charged leptons; the interaction

¹For simplicity, we have assumed universal couplings for different lepton flavors.

Lagrangian is given by

$$\mathcal{L} = Z'_\mu \bar{\chi} \gamma^\mu (g_v^\chi - g_a^\chi \gamma_5) \chi + Z'_\mu \bar{\ell} \gamma^\mu (g_v^\ell - g_a^\ell \gamma_5) \ell, \quad (2.5)$$

where Z' denotes the light mediator, χ is the dark matter, ℓ is the SM charged lepton, $g_v^{\chi,\ell}$ ($g_a^{\chi,\ell}$) is the vector (axial-vector) coupling. The mono-photon cross section at the electron colliders for the process $e^+e^- \rightarrow \gamma Z' \rightarrow \gamma \chi \bar{\chi}$ is given by [51]

$$\begin{aligned} \frac{d\sigma}{dE_\gamma dz_\gamma} &= \frac{\alpha s_\gamma^2 \left[(g_v^\ell)^2 + (g_a^\ell)^2 \right]}{6\pi^2 s E_\gamma \left[(s_\gamma - m_{Z'}^2)^2 + m_{Z'}^2 \Gamma_{Z'}^2 \right]} \sqrt{1 - 4 \frac{m_\chi^2}{s_\gamma}} \left[1 + \frac{E_\gamma^2}{s_\gamma} (1 + z_\gamma^2) \right] \frac{1}{1 - z_\gamma^2} \\ &\times \left[(g_v^\chi)^2 \left(1 + 2 \frac{m_\chi^2}{s_\gamma} \right) + (g_a^\chi)^2 \left(1 - 4 \frac{m_\chi^2}{s_\gamma} \right) \right], \end{aligned} \quad (2.6)$$

where E_γ and θ_γ are the photon energy and polar angle respectively in the center of mass frame, s is the square of the center of mass energy, $z_\gamma = \cos \theta_\gamma$, $s_\gamma = s - 2\sqrt{s}E_\gamma$, and $m_{Z'}$ and $\Gamma_{Z'}$ are the mass and the total decay width of the Z' boson. The Z' total decay width is given by

$$\Gamma_{Z'} = \Gamma(Z' \rightarrow \chi \bar{\chi}) + \sum_\ell \Gamma(Z' \rightarrow \ell \bar{\ell}), \quad (2.7)$$

where $\Gamma(Z' \rightarrow \chi \bar{\chi})$ is the invisible decay width with DM in the final state, and $\Gamma(Z' \rightarrow \ell \bar{\ell})$ is the decay width with SM particles in the final state. The invisible decay width is given by

$$\Gamma(Z' \rightarrow \chi \bar{\chi}) = \frac{m_{Z'}}{12\pi} \sqrt{1 - 4 \frac{m_\chi^2}{m_{Z'}^2}} \left[(g_v^\chi)^2 \left(1 + 2 \frac{m_\chi^2}{m_{Z'}^2} \right) + (g_a^\chi)^2 \left(1 - 4 \frac{m_\chi^2}{m_{Z'}^2} \right) \right], \quad (2.8)$$

$\Gamma(Z' \rightarrow \ell \bar{\ell})$ can be computed similarly by substituting the couplings and mass for lepton.

3 Mono-photon searches at Belle II

In this section, we use the mono-photon final state, $e^+e^- \rightarrow \chi \bar{\chi} \gamma$, to probe the DM models at Belle II. For each of the DM models, the number of signal events is calculated by the analytic expressions of the differential cross sections offered in section 2. In our analysis, we consider both the reducible background and the irreducible background for the mono-photon process.

The mono-photon irreducible background is due to the $e^+e^- \rightarrow \gamma \nu \bar{\nu}$ process in the SM; the differential cross section of the $e^+e^- \rightarrow \gamma \nu \bar{\nu}$ process in the SM is given by [44, 69, 70]

$$\frac{d\sigma_{\nu\bar{\nu}\gamma}}{dE_\gamma dz_\gamma} = \frac{\alpha G_F^2 s_\gamma^2}{4\pi^2 s E_\gamma (1 - z_\gamma^2)} \left[8s_W^4 - \frac{4}{3}s_W^2 + 1 \right] \left[1 + \frac{E_\gamma^2}{s_\gamma} (1 + z_\gamma^2) \right], \quad (3.1)$$

where G_F is the Fermi constant, $s_W \equiv \sin \theta_W$ with θ_W being the weak mixing angle.

Photons at Belle II are detected in the ECL and KLM sub-detectors, both of which consist of three segments: the forward detector, the backward detector, and the barrel

detector [24]. The mono-photon reducible backgrounds at the Belle II detector come from the SM processes in which one or more SM final state particles are not detected by the detector. The main reducible background in our analysis is due to the $e^+e^- \rightarrow \gamma\cancel{\gamma}\cancel{\gamma}$ process,² where two of the final state photons are not detected because one photon escapes in the beam direction and the other escapes in the region where the detector has no coverage or a very low detection efficiency, for example, the gaps between different segments of the ECL and KLM sub-detectors, and the gap located at 90° of the ECL barrel [24].³

The reducible BG at the Belle II detector has been analyzed by Ref. [24]. For the sub-GeV DM particles, we adopt the low-mass region given in Ref. [24] as the signal region in our analysis; recently a fitting function for the boundary of this region is given in Ref. [27]

$$\theta_{\min}^{\text{low}} = 5.399^\circ E_{\text{CMS}}(\gamma)^2/\text{GeV}^2 - 58.82^\circ E_{\text{CMS}}(\gamma)/\text{GeV} + 195.71^\circ, \quad (3.2)$$

$$\theta_{\max}^{\text{low}} = -7.982^\circ E_{\text{CMS}}(\gamma)^2/\text{GeV}^2 + 87.77^\circ E_{\text{CMS}}(\gamma)/\text{GeV} - 120.6^\circ, \quad (3.3)$$

where $\theta_{\min}^{\text{low}}$ and $\theta_{\max}^{\text{low}}$ are the minimum and maximum angles for the photon in the lab frame, namely $\theta_{\min}^{\text{low}} < \theta_{\gamma}^{\text{lab}} < \theta_{\max}^{\text{low}}$.⁴ In the signal region, about 300 mono-photon events from the reducible backgrounds are expected with 20 fb^{-1} data [24], corresponding to $\sim 7.5 \times 10^5$ mono-photon events with 50 ab^{-1} data; there are about 1.9×10^3 mono-photon events from the irreducible background process $e^+e^- \rightarrow \nu\bar{\nu}\gamma$ with 50 ab^{-1} data.

4 Mono-photon constraints on EFT operators

We compute the Belle II 90% C.L. limits on the EFT operators, by using the criterion $N_s/\sqrt{N_b} = \sqrt{2.71}$, where N_s (N_b) is the number of signal (background) events in the signal region. Fig. (1) shows the Belle II 90% C.L. lower bounds on the new physics scale Λ of the EFT operators, from the mono-photon channel with 50 ab^{-1} integrated luminosity. As shown in the left panel figure of Fig. (1), the Belle II 90% C.L. lower bounds are ~ 280 GeV, for Λ_V , Λ_A , and Λ_s , and are about ~ 220 GeV for Λ_t . We further compare the Belle II limits to the LEP limits analyzed by Ref. [39]. Mono-photon data with 650 pb^{-1} at various \sqrt{s} from 180 GeV to 209 GeV have been collected by the DELPHI detector at LEP [39, 71]. The LEP mono-photon data are binned in 19 $x_\gamma = E_\gamma/E_{\text{beam}}$ bins [39], where E_γ and E_{beam} are the energy of photon and the beam energy respectively. The LEP 90% C.L. lower limits on EFT operator with sub-GeV mass, are about 480 GeV for Λ_V and Λ_A , 440 GeV for Λ_s , and 340 GeV for Λ_t [39].

Although the expected integrated luminosity of Belle II is about five orders of magnitude larger than LEP, their limits on the EFT operators turn out to be of similar size. This is largely due to the fact that EFT operators and the SM processes depend on \sqrt{s} in different ways. For the four-fermion EFT operators, the cross section is proportional to s (to

²We use “slash” to denote a particle that is not detected by the detector.

³The reducible BG due to $e^+e^- \rightarrow \gamma\cancel{\ell}^+\cancel{\ell}^-$ is subdominant, because charged leptons can either be detected by tracking detectors if emitted in the central region [24], or be effectively removed by kinematic conditions if emitted along the beam directions [26].

⁴We use “lab” to denote the variable in the lab frame.

compensate the Λ^4 factor in the denominator), whereas for the QED process (responsible for the reducible background at Belle II), the cross section is inversely proportional to s . For that reason, the dominant reducible background at Belle II becomes totally negligible at LEP, whereas the cross sections of EFT operators at LEP are enhanced by a factor of ~ 400 as compared to Belle II. The weak processes that lead to the irreducible mono-photon backgrounds have a similar proportionality on s as the EFT operators up to the Z/W mass scale. Taking these effects into consideration, we find that LEP is expected to have similar constraints on the four-fermion EFT operators as Belle II.

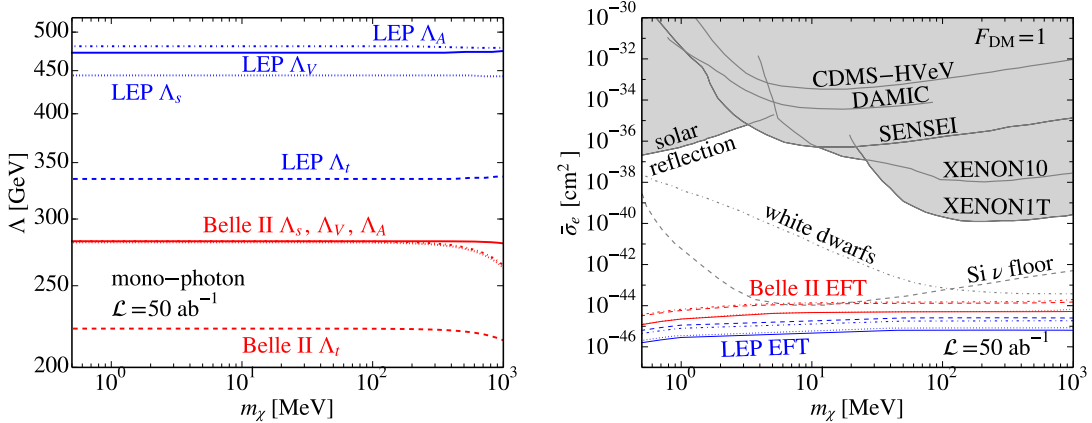


Figure 1. Left panel: Belle II 90% C.L. lower bounds (red curves) on the new physics scale Λ_A (dot-dashed), Λ_V (solid), Λ_s (dotted), and Λ_t (dashed), in the EFT operators as a function of the DM mass, via the mono-photon channel with the integrated luminosity 50 ab^{-1} . The LEP constraints (blue curves) [39] with the luminosity of 650 pb^{-1} are also shown. Right panel: Belle II and LEP constraints on the DM-electron cross section at the reference momentum $q = \alpha m_e$ for the EFT operators, as well as constraints from DMD experiments with $F_{\text{DM}}(q) = 1$, including XENON10 [5], CDMS-HVeV [72], XENON1T [6], DAMIC [73], and SENSEI [74]. Constraints for boosted DM from solar reflection [22] and constraints on dark matter capture in white dwarfs are also shown. We compute the white dwarf limit at the reference momentum $q = \alpha m_e$ by using the lower bound on Λ given in Ref. [13]. The dashed gray line shows the neutrino floor limit for silicon target detectors where the exposure is 1000 kg-year [75].

We further compare the collider constraints on the EFT operators to other experimental constraints. We compute the DM-electron scattering cross section at the momentum transfer $q \equiv |\mathbf{q}| = \alpha m_e$ [76, 77], by using the limit on Λ in the EFT operators

$$\bar{\sigma}_e \equiv \frac{\mu_{\chi e}^2}{16\pi m_\chi^2 m_e^2} \overline{|\mathcal{M}_{\chi e}(q)|^2} \Big|_{q=\alpha m_e}, \quad (4.1)$$

where m_χ is the DM mass, m_e is the electron mass, $\mu_{\chi e}$ is the reduced mass. Here both DM and electron are assumed to be non-relativistic, and the dependence on q is solely in the matrix element $\mathcal{M}_{\chi e}$, which can be factorized as $|\mathcal{M}_{\chi e}(q)|^2 = |\mathcal{M}_{\chi e}(\alpha m_e)|^2 |F_{\text{DM}}(q)|^2$. We have $|\mathcal{M}_{\chi e}(\alpha m_e)|^2 \simeq 16m_e^2 m_\chi^2 / \Lambda^4$ for all the four EFT operators except Λ_A which is 3 times larger. The form factor for the EFT operators considered in our analysis is found

to be $F_{\text{DM}}(q) \simeq 1$.⁵ For the EFT operators the collider constraints from Belle II and LEP on sub-GeV DM are found to be much stronger than the DMDD limits, including the constraints from SENSEI [74], CDMS-HVeV [72], DAMIC [73], XENON10 [5], XENON1T [6], DMDD limits via solar reflection [22], and white dwarfs [13–18]. The constraint on $\bar{\sigma}_e$ from white dwarfs, as shown in Fig. (1), is computed via Eq. (4.1), by using of the lower bound on $\Lambda_V \simeq 200$ GeV in Ref. [13].⁶ Signals due to neutrino-target scatterings are the irreducible background in DMDD, which are often referred to as the neutrino floor. The gray dashed line in Fig. (1) shows the neutrino floor for Si detectors with a 1000 kg-year exposure [75].⁷ Thus, it is remarkable that LEP and Belle II can probe the parameter space beyond the neutrino floor, especially in the sub-MeV mass region, as shown in Fig. (1). We note that the DMDD limits are the same for all the four EFT operators, since $F_{\text{DM}}(q) = 1$ is used, but the collider limits are slightly different for the four EFT operators. Thus the electron collider constraints, from Belle II and LEP, can further extend to the sub-MeV DM region where many of the current direct detection experiments lose sensitivity due to the low recoil energy.

5 Mono-photon constraints on light mediator model

We investigate the capability of the Belle II detector in probing the light mediator models in which the light mediator Z' couples to both DM and charged leptons. Unlike the four-fermion EFT operators, the collider cross section in the light-mediator models is not proportional to s . For that reason, the Belle II is expected to explore some new parameter space in the light-mediator models that has not been probed by the LEP experiment.

In this analysis, we are interested in the Z' mass below the Belle II $\sqrt{s} \simeq 10$ GeV. Thus we consider three Z' masses in the MeV-GeV mass range: 10 MeV, 0.6 GeV, and 5 GeV. We note that for ultralight mediators, constraints from cosmic microwave background (CMB) and baryon acoustic oscillations (BAO) are usually much more stringent than collider searches [79].

We compute the Belle II 90% C.L. limits on the light-mediator models using the same criterion as the EFT operators, namely by setting $N_s/\sqrt{N_b} = \sqrt{2.71}$, where N_s is obtained by integrating Eq. (2.6) in the signal region. The expected Belle II 90% C.L. upper bounds with 50 ab^{-1} data on the gauge coupling are shown on left panel figure of Fig. (2) and Fig. (3), where we only consider vector couplings and axial-vector couplings respectively. The collider signals depend strongly on the mass relations between the light mediator and DM. There are two categories:

- $m_{Z'} > 2m_\chi$. The Z' boson mainly decays into dark matter. Thus the Z' boson can be produced on-shell in the $e^+e^- \rightarrow \chi\bar{\chi}\gamma$ process and is exhibited as a resonance in

⁵See appendix C for the expressions of $|\mathcal{M}_{\chi e}(q)|^2$ for the EFT operators and also the range of $F_{\text{DM}}(q)$ for the momentum of interest.

⁶Our white dwarf constraint on $\bar{\sigma}_e$ is different from Ref. [13] where the cross section is evaluated at the momentum/energy scale relevant for DM captures in white dwarfs [78]. The white dwarfs limits are $\Lambda_V \simeq \Lambda_A \simeq 200$ GeV and $\Lambda_s \simeq 200$ MeV when $m_\chi > 100$ MeV as given in Ref. [13].

⁷The neutrino floors for Xe and Ge targets are higher than Si.

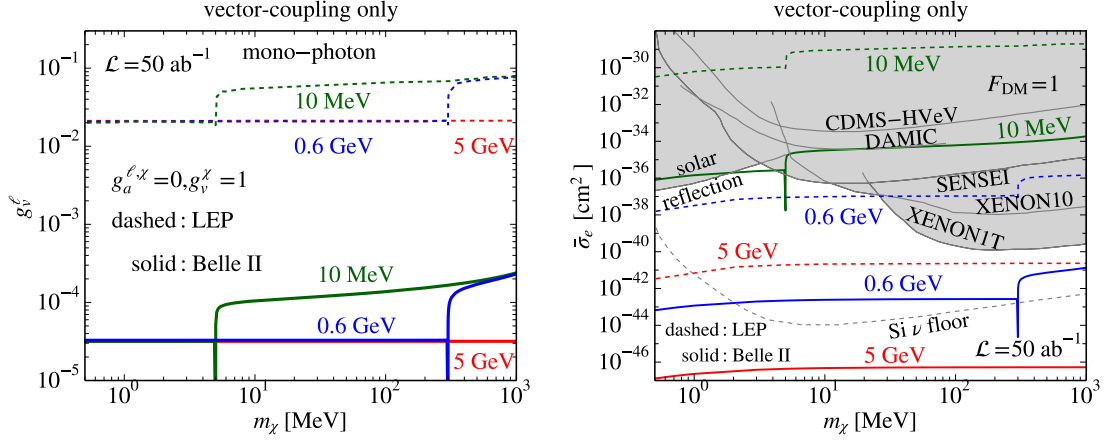


Figure 2. The expected Belle II 90% upper bound (solid lines) with 50 ab^{-1} integrated luminosity on g_v^l (left panel) and $\bar{\sigma}_e$ (right panel) in light mediator models where only vector couplings are assumed. Three Z' masses are considered for the Belle II analysis: $m_{Z'} = 5 \text{ GeV}$ (red), $m_{Z'} = 0.6 \text{ GeV}$ (blue), and $m_{Z'} = 10 \text{ MeV}$ (green). The LEP constraints (dashed lines) with 650 pb^{-1} integrated luminosity are also shown for two Z' masses: $m_{Z'} = 5 \text{ GeV}$ (red), and $m_{Z'} = 0.6 \text{ GeV}$ (blue), and $m_{Z'} = 10 \text{ MeV}$ (green). Constraints from DMDD experiments with $F_{\text{DM}}(q) = 1$ (valid for $m_{Z'} \gg \alpha m_e$) are also shown: SENSEI [74], XENON10 [5] and XENON1T [6], CDMS-HVeV [72], DAMIC [73], and solar reflection [22]. The gray dashed line shows the neutrino floor limit for silicon detectors [75].

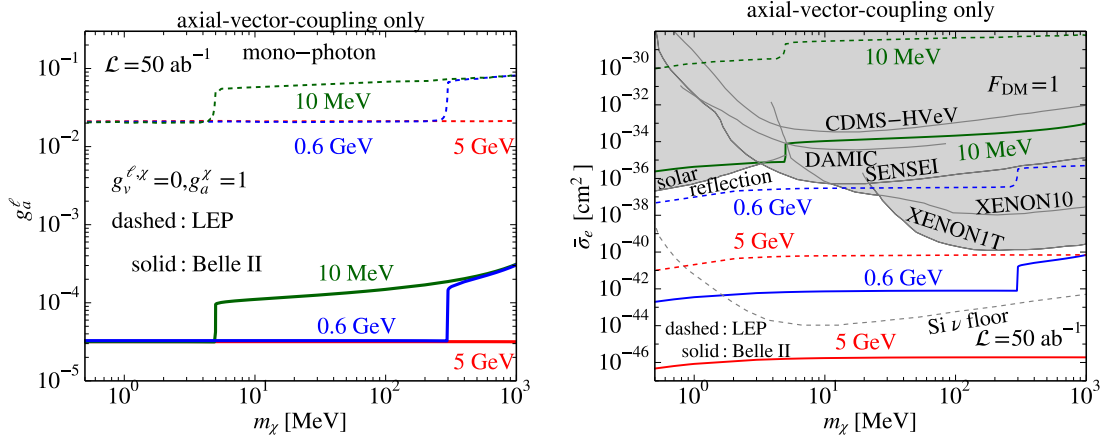


Figure 3. Same as Fig. (2) but for light mediator models where only axial-vector couplings are assumed.

the mono-photon energy spectrum (see e.g. [42, 43, 51, 55]). The mono-photon cross section can be approximated by $\sigma_{\chi\bar{\chi}\gamma} \simeq \sigma_{\gamma Z'} \times \text{BR}(Z' \rightarrow \chi\bar{\chi})$. Because the branching ratio $\text{BR}(Z' \rightarrow \chi\bar{\chi}) \simeq 1$ in the parameter space of interest in this analysis, and the cross section $\sigma_{\gamma Z'}$ is proportional to $(g^\ell)^2$, the mono-photon cross section depends on g^ℓ , but not on m_χ or g^X . The m_χ independence can be seen in Fig. (2) and Fig. (3) in the mass range $m_\chi < m_{Z'}/2$.

- $m_{Z'} < 2m_\chi$. The Z' boson can only decay into the SM particles. Thus the Z' boson is produced off-shell in the $e^+e^- \rightarrow \chi\bar{\chi}\gamma$ process without a resonance in the mono-photon energy spectrum. In this case, $\sigma_{\chi\bar{\chi}\gamma}$ is proportional to $(g_\ell g_\chi)^2$ and depends on m_χ , which can be seen in Fig. (2) and Fig. (3).

For both the vector-only case and the axial-vector-only case, the Belle II upper limits are about $g^\ell \sim 3 \times 10^{-5}$ when $m_{Z'} > 2m_\chi$, as shown in Fig. (2) and Fig. (3). For the vector-only case, the sensitivity is highly enhanced if $m_{Z'} = 2m_\chi$. We further compare the Belle II limits to the LEP limits. LEP constraints on light mediator models with $m_{Z'} \geq 10$ GeV have been studied in Ref. [39]. Here we analyze the LEP constraints to the region where $m_{Z'} < 10$ GeV, following the analysis of Ref. [39]; the details of our LEP analysis are given in section D. As shown in Fig. (2) and Fig. (3), the LEP constraints are about 3×10^{-2} for both vector and axial-vector couplings when $m_{Z'} > 2m_\chi$, which are three orders of magnitude weaker than Belle II. Unlike the EFT operators, there are resonance signals in the mono-photon energy spectrum, which correspond to the Breit-Wigner resonance of the Z' boson, in the light mediator models. One could select the events near the resonance to further improve the significance of the searches. We have not taken advantage of this, because such a study requires the detailed knowledge of the subdetectors to simulate the reducible background, which, however, is beyond the scope of this study.

Similar to the analysis for the EFT operators, we compare the collider limits on the light mediator models to DMDD limits on the right panel figures of Figs. (2) and (3). In the non-relativistic limit, the amplitude for the light mediator models is given by

$$|\overline{\mathcal{M}_{\chi e}}|^2 \simeq 16m_e^2 m_\chi^2 \frac{(g_v^\ell g_v^X)^2 + 3(g_a^\ell g_a^X)^2}{(m_{Z'}^2 + q^2)^2}. \quad (5.1)$$

Thus we have $F_{\text{DM}}(q) \simeq 1$ for $m_{Z'} \gg \alpha m_e$, which is the case for the model points considered in our study. The reference amplitude $|\overline{\mathcal{M}_{\chi e}(q = \alpha m_e)}|^2$ is obtained by neglecting q^2 term in the denominator of Eq. (5.1), resulting in an $m_{Z'}^{-4}$ dependence in the reference cross section $\bar{\sigma}_e$. We find that for the light mediator in the GeV scale, the Belle II limits can be several orders of magnitude stronger than the DMDD limits, including SENSEI [74], CDMS-HVeV [72], DAMIC [73], XENON10 [5], XENON1T [6], and DMDD limits via solar reflection [22]. For example, Belle II can explore the parameter space well below the neutrino floor for silicon detectors [75], for the case where $m_{Z'} \gtrsim 5$ GeV. However, for the mediator mass at the MeV scale, the Belle II limits become somewhat weaker due to the $m_{Z'}^{-4}$ dependence. For example, the parameter space to be probed by Belle II for the $m_{Z'} \sim 10$ MeV case has already been excluded by the current DMDD limits, except the parameter space in

the vicinity of $m_{Z'} \simeq 2m_\chi$ in the vector-coupling-only case, where the Belle II limits are significantly enhanced.

A meta-stable particle that decays into SM particles are constrained by BBN bounds. Ref. [80] finds that the upper bound on the lifetime of the meta-stable particle that decays into electron and/or photon final states must be less than $\sim 10^{-1}$ (10^3) sec if the mass is about 1 GeV (MeV), in order to satisfy the BBN bound. As shown in Figs. (2) and (3), the smallest vector/axial-vector coupling probed by Belle II is about $g^\ell \simeq \mathcal{O}(10^{-5})$, leading to a lifetime of $\tau \simeq \mathcal{O}(10^{-13})$ sec for $m_{Z'} \sim 1$ GeV and $\tau \simeq \mathcal{O}(10^{-10})$ sec for $m_{Z'} \sim 1$ MeV, which are much smaller than the BBN bounds. Thus, the BBN bounds on the light vector mediator models considered in this study are much weaker than the Belle II sensitivities.

We further display the Belle II mono-photon constraints on $\bar{\sigma}_e$ with 50 ab^{-1} for each model point in the $m_\chi - m_{Z'}$ plane for the vector-coupling-only case, as shown in Fig. (4). Because the $\bar{\sigma}_e$ value to be probed by Belle II is proportional to $m_{Z'}^{-4}$, the DM models with a smaller $m_{Z'}$ is less constrained, for example $\bar{\sigma}_e > 10^{-30} \text{ cm}^2$ is still allowed for a sub-MeV mediator. We also find that the constraint decreases with the DM mass m_χ and becomes very strong in the vicinity of the $m_{Z'} = 2m_\chi$ line.

Recently, excess events in the electron recoil data are observed in the Xenon1T experiment [61]. A number of papers have used DM to explain such an excess, some of which require a sizable DM-electron interaction cross section [81–84]. We note that for EFT operators between DM and electron, and for the GeV-mediator models, such strong DM-electron interaction cross sections are likely to be constrained by Belle II. However, for the models with a relatively light mediator, the DM-electron cross section can be significantly large, for example, $\bar{\sigma}_e \gtrsim \mathcal{O}(10^{-30}) \text{ cm}^2$ for the mediator mass below MeV is likely to remain unconstrained with the Belle II data.

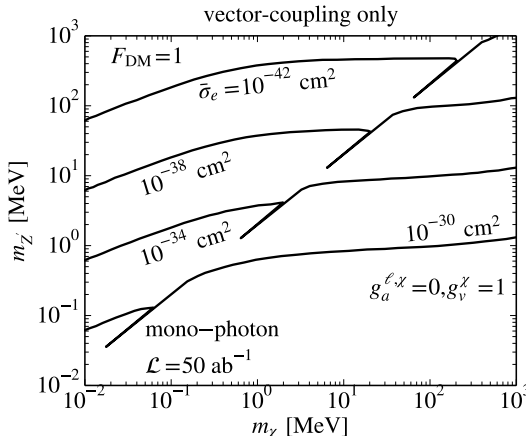


Figure 4. The expected Belle II upper bound on $\bar{\sigma}_e$ for each model point in the $m_\chi - m_{Z'}$ plane, in the mono-photon channel with 50 ab^{-1} , where only vector couplings are considered. We have estimated the limits in the vicinity of $m_{Z'} = 2m_\chi$, where the Belle II sensitivity is highly enhanced. The limits along the $m_{Z'} = 2m_\chi$ line are shown for illustrative purposes only; the more accurate values require a detailed analysis which is beyond the scope of the current work.

6 Di-lepton constraints on light mediator models

Because for the light mediator that couples to leptons, it is inevitable that the mediator can decay into a pair of final state leptons if kinematically allowed, one can search for the dark matter via the visible decay of the light mediator. Here we choose the process $e^+e^- \rightarrow \gamma\mu^+\mu^-$ to search for the Z' resonance in the di-muon invariant mass spectrum.⁸ We consider the following two Z' masses: $m_{Z'} = 0.6$ GeV and $m_{Z'} = 5$ GeV.

We use MADGRAPH [86] to generate 10^5 events for the $e^+e^- \rightarrow \gamma\mu^+\mu^-$ process for each new physics model point and for the SM. The main SM backgrounds are from $e^+e^- \rightarrow \gamma\mu^+\mu^-$ mediated by photon, since the center of mass energy is much smaller than the mass of Z boson. We use the following preselection cut for MADGRAPH simulations: we select photons that are within the angle coverage of ECL such that $12.4^\circ < \theta_\gamma^{\text{lab}} < 155.1^\circ$, and muons within the angle coverage of KLM such that $25^\circ < \theta_{\mu^\pm}^{\text{lab}} < 155^\circ$ [24]. We adopt the “three isolated clusters” [28] as the trigger condition, which requires that (i) at least three isolated calorimeter clusters with a minimum distance of $d_{\text{min}} = 30$ cm;⁹ (ii) at least one of the three clusters needs to have $E_{\text{lab}} > 0.5$ GeV and the two additional clusters $E_{\text{lab}} > 0.18$ GeV; (iii) all three clusters need to have $18.5^\circ \leq \theta_{\text{lab}} \leq 139.3^\circ$. We apply the isolation cuts to the photon and muon events that are simulated via MADGRAPH. For the triggered events, we follow Ref. [27] to apply the selection cuts for muons and photons as follows. We select a pair of muons such that (i) both $p_T(\mu^+)$ and $p_T(\mu^-) > 0.05$ GeV, (ii) the opening angle of the muon pair is larger than 0.1 rad, and (iii) the invariant mass of the muon pair $m_{\mu\mu} > 0.03$ GeV.¹⁰ We select photons that satisfy $E_{\text{lab}} > 0.5$ GeV and $17^\circ \leq \theta_{\text{lab}} \leq 150^\circ$.

To search for the Z' resonance, we further apply a detector cut of $|m_{\mu\mu} - m_{Z'}| < 2 \max\{\Gamma_{Z'}, \sigma_{m_{\mu\mu}}\}$, where $m_{\mu\mu}$ is the reconstructed di-muon invariant mass, and $\sigma_{m_{\mu\mu}}$ is its uncertainty. The resonant mass resolution is $\sim 0.2\%$ for charmonium and 0.3% for bottomonium resonances [24]. In our analysis, we adopt a constant resolution as $\sigma_{m_{\mu\mu}} = 0.01$ GeV for the di-muon invariant mass measurement, since we are primarily interested in the light mediators.¹¹ To our knowledge, the two Z' masses considered here do not coincide with any significant di-muon backgrounds from hadron decays. Otherwise a more sophisticated study is in order. We note that taking into account the angular distributions of the final state particles does not improve the sensitivities, because the new physics process

⁸Another di-lepton invariant mass channel is $e^+e^- \rightarrow \gamma e^+e^-$, which, however, has a much larger background due to an additional t -channel diagram and the photon conversion process in the low invariant mass region [85]. Therefore, we do not consider $e^+e^- \rightarrow \gamma e^+e^-$ in this study.

⁹We use the incident position on the first layer of the ECL detectors to compute d_{min} . The inner surface of the barrel region of the detector is $r = 125$ cm away from the beam and with the polar angle $32.2^\circ < \theta < 128.7^\circ$; the forward (backward) detector is placed at $z = +196$ (-102) cm with $12.4^\circ < \theta < 31.4^\circ$ ($130.7^\circ < \theta < 155.1^\circ$) [24].

¹⁰The invariant mass cut $m_{\mu\mu} > 30$ MeV hinders the di-muon sensitivities to very light mediators, e.g., the $m_{Z'} = 10$ MeV case as analyzed in the mono-photon channel.

¹¹In the $e^+e^- \rightarrow \gamma\mu^+\mu^-$ process at the electron colliders, one can determine the di-muon invariant mass by using the measured photon energy via $m_{\mu\mu}^2 = s - 2\sqrt{s}E_\gamma$, and the uncertainty is given by $\sigma_{m_{\mu\mu}} = \sigma_{E_\gamma}\sqrt{s}/m_{\mu\mu}$, where $\sigma_{E_\gamma}/E_\gamma = 2\%$ [24]. In the $m_{Z'} = 5$ GeV case, we have $\sigma_{m_{\mu\mu}}/m_{\mu\mu} \simeq 3.4\%$ from the photon energy measurement, which is much larger than the di-muon channel. Hence, the di-muon channel has a better resolution for a narrow Z' resonance than the mono-photon channel.

has a similar di-muon angular distribution as the SM background.

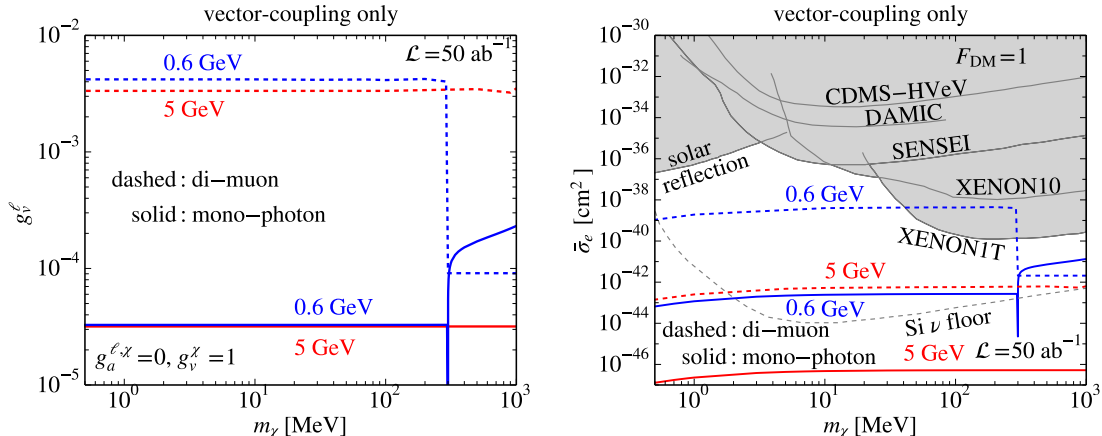


Figure 5. The expected Belle II 90% C.L. upper bound via visible search (dashed) with 50 ab^{-1} integrated luminosity on g_v^ℓ (left panel) and $\bar{\sigma}_e$ (right panel) in light mediator models where only vector couplings are assumed. Two Z' masses are considered for the di-muon search analysis: $m_{Z'} = 5 \text{ GeV}$ (red) and $m_{Z'} = 0.6 \text{ GeV}$ (blue). The Belle II mono-photon search constraints (solid) are shown for the two Z' masses. Constraints from DMDD experiments with $F_{\text{DM}}(q) = 1$ (valid for $m_{Z'} \gg \alpha m_e$) are also shown: SENSEI [74], XENON10 [5] and XENON1T [6], CDMS-HVeV [72], DAMIC [73], and solar reflection [22]. The gray dashed line shows the neutrino floor limit for silicon detectors [75].

We compute the Belle II sensitivity (90% C.L. upper bound) to the new physics model in the di-muon channel with 50 ab^{-1} integrated luminosity, by using the condition $N_s/\sqrt{N_b} = \sqrt{2.71}$, where N_s is the number of new physics signal events, and N_b is the number of SM background events. The expected 90% C.L. upper bounds on g_v^ℓ are shown on the left panel figure of Fig. (5) where we take $g_a^\ell = g_a^\chi = 0$ and $g_v^\chi = 1$; the corresponding limits on $\bar{\sigma}_e$ are shown on the right panel figure of Fig. (5). For the $m_{Z'} = 5 \text{ GeV}$ case, the expected 90% C.L. upper bound on g_v^ℓ in the di-muon channel is $g_v^\ell \lesssim 3 \times 10^{-3}$ in the MeV-GeV DM mass range, which is about two orders of magnitude weaker than in the mono-photon channel. The $m_{Z'} = 0.6 \text{ GeV}$ case is similar to the $m_{Z'} = 5 \text{ GeV}$ except in the mass range $m_\chi > 0.3 \text{ GeV}$, where the di-muon limit becomes stronger than the mono-photon limit. This is due to the fact that for the case where $m_{Z'} = 0.6 \text{ GeV}$ and $m_\chi > 0.3 \text{ GeV}$, di-leptons can be produced on the Z' resonance, but DM can only be produced off the Z' resonance. The di-muon limit for the $m_{Z'} = 5 \text{ GeV}$ case is comparable to the neutrino floor limit of the silicon detectors [75] and is several orders of magnitude stronger than the current DMDD limits, which includes SENSEI [74], XENON10 [5] and XENON1T [6], CDMS-HVeV [72], DAMIC [73], and solar reflection [22], as shown in the right panel figure of Fig. (5). The di-muon limit for the $m_{Z'} = 0.6 \text{ GeV}$ case is stronger than the current DMDD limits except the mass range of $20 \text{ MeV} \lesssim m_\chi \lesssim 300 \text{ MeV}$ where XENON1T [6] becomes stronger.

The expected 90% C.L. upper bounds on g_a^ℓ are shown on the left panel figure of Fig. (6) where we take $g_v^\ell = g_v^\chi = 0$ and $g_a^\chi = 1$; the corresponding limits on $\bar{\sigma}_e$ are shown on the right panel figure of Fig. (6). The di-muon limit on g_a^ℓ is about three times weaker than

g_v^ℓ in the low DM mass range.

The different limits on g_a^ℓ and g_v^ℓ are primarily due to different behaviors in the photon- Z' interference terms in the cross section. The total amplitude square of the $e^+e^- \rightarrow \mu^+\mu^-\gamma$ process can be parameterized as $|\mathcal{M}|^2 = |\mathcal{M}_\gamma + \mathcal{M}_{Z'} + \mathcal{M}_Z|^2$, where \mathcal{M}_γ , $\mathcal{M}_{Z'}$, and \mathcal{M}_Z denote the amplitudes mediated by the photon, Z' , and Z respectively. Since m_Z is much larger than \sqrt{s} of Belle II, we neglect \mathcal{M}_Z here. Hence, the $e^+e^- \rightarrow \mu^+\mu^-\gamma$ cross section receives three contributions: $\sigma = \sigma_\gamma + \sigma_{\gamma Z'} + \sigma_{Z'}$, where σ_γ denotes the SM background mediated by the photon, $\sigma_{\gamma Z'}$ denotes the cross section due to the $\gamma - Z'$ interference term, and $\sigma_{Z'}$ denotes the cross section due to the Z' term. The expressions of $\sigma_{Z'}$ are similar in the vector only case and in the axial-vector only case; the $\sigma_{\gamma Z'}$ contributions, however, are very different. For example, we have $\sigma_{\gamma Z'} = 2.36$ (-0.379) fb and $\sigma_{Z'} = 0.472$ (0.603) fb for the case where g_v^ℓ (g_a^ℓ) = 0.01, $m_{Z'} = 5$ GeV, and $m_\chi = 1$ GeV. Therefore the total cross section in the vector case is about one order of magnitude larger than the axial-vector case. Although we have imposed detector cuts to select events from the Z' resonance, the contribution from $\sigma_{\gamma Z'}$ turns out to be comparable to that from $\sigma_{Z'}$, because the NP couplings (g_v^ℓ and g_a^ℓ) are much smaller than the QED coupling constant e .

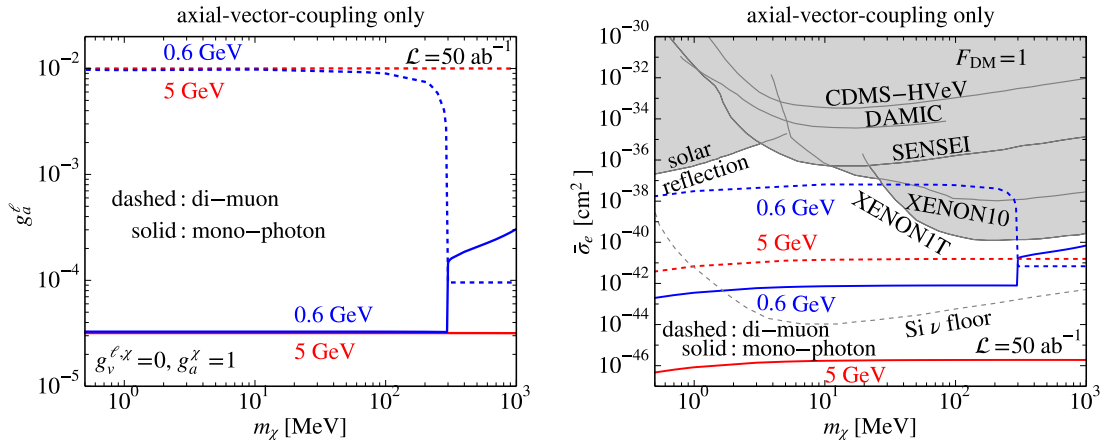


Figure 6. Same as Fig. (5) but where only axial-vector coupling are assumed.

We further compare the 90% C.L. upper bound on g_v^ℓ from the mono-photon channel and from the di-muon channel on the $g_v^\chi - g_v^\ell$ plane in Fig. (7), where we consider the vector-only case and take $m_{Z'} = 0.6$ GeV. For the case where $m_\chi = 0.1$ GeV, the Z' boson can decay into a pair of DM particles. For that reason, Belle II can probe a much smaller g_v^ℓ in the mono-photon channel than in the di-muon channel, in the range of $g_v^\ell \gtrsim 5 \times 10^{-5}$; only for very small g_v^χ values (namely $g_v^\chi \lesssim 5 \times 10^{-5}$), the di-muon channel becomes the better channel to constrain the parameter space. We further compare the sensitivities from these two channels for all the model points on the $g_v^\ell - g_v^\chi$ plane, and find that the parameter space can be approximately divided by the line $g_v^\ell = 2g_v^\chi$ into two regions: model points on the left-upper side of the line typically receive a stronger constraint from the di-muon channel than from the mono-photon channel; model points on the right-lower side of the line, on the other hand, are better constrained by the mono-photon channel. We also estimate the

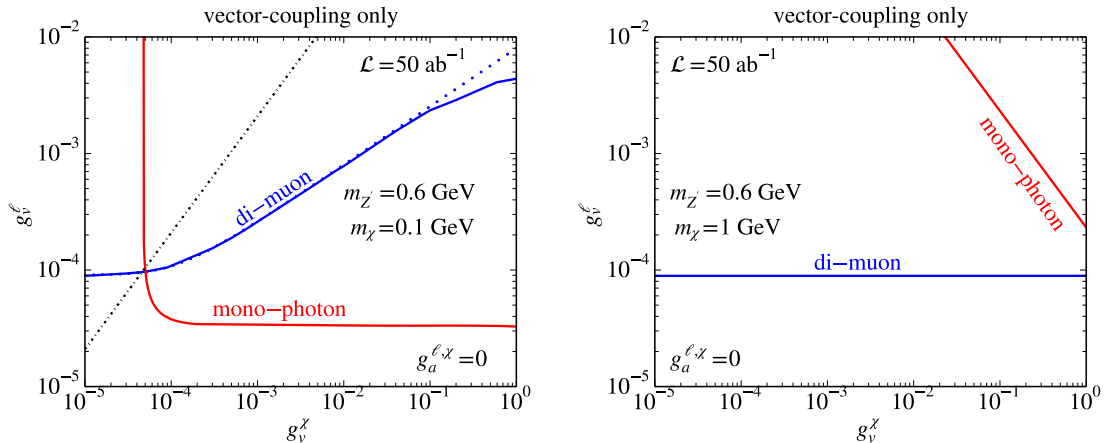


Figure 7. Left panel: Expected Belle II 90% C.L. upper bound on g_v^ℓ as a function of g_v^x from the di-muon channel (blue) and from the mono-photon channel (red) with 50 ab^{-1} integrated luminosity, $m_{Z'} = 0.6 \text{ GeV}$, $m_\chi = 0.1 \text{ GeV}$, and only vector couplings. The parameter space, where the sensitivity of the visible channel is the same as the invisible channel, is approximated by the black dot-dashed line, which is $g_v^\ell = 2g_v^x$. The upper bound in the di-muon channel estimated by neglecting the $\gamma - Z'$ interference term is indicated by the blue dotted line. Right panel: same as the left panel but with $m_\chi = 1 \text{ GeV}$.

di-muon sensitivity curve by neglecting the $\gamma - Z'$ interference term, as indicated by the blue dotted line in the left panel figure of Fig. (7). We find that the $\gamma - Z'$ interference term cannot be neglected for the parameter range of $g_v^x > 0.1$ and produces the dominant contribution to the di-muon signal for the parameter range of $g_v^x \sim 1$ (in the vicinity of the sensitivity curve).

For the case where $m_\chi = 1 \text{ GeV}$, the Z' boson cannot decay into a pair of DM particles. For that reason, the sensitivity on g_v^ℓ from the di-muon channel is always better than the mono-photon channel for the entire g_v^x range shown in the right panel figure of Fig. (7). We also find that the di-muon limits in the $m_\chi = 1 \text{ GeV}$ case are better than the $m_\chi = 0.1 \text{ GeV}$ case, since in the former case the Z' boson can only decay into visible final states.

7 NA64 constraints

Light dark matter that couples to electron can also be searched for at the NA64 experiment, an electron fixed target experiment with a lead target. The energy of the incident electron of the NA64 experiment is 100 GeV [62]. In this section, we compute the constraints on the EFT operators and on the light mediator models, by using the 2.84×10^{11} electrons on target (EOT) data accumulated by the NA64 experiment [62].

A pair of fermionic DM can be produced at NA64 via a 2-to-4 process

$$e^-(p) + N(P_i) \rightarrow e^-(p') + N(P_f) + \chi(k_1) + \bar{\chi}(k_2), \quad (7.1)$$

where N is the Pb nucleus, and we have specified the momentum for each particle in the parenthesis. The DM signature is a large missing energy carried away by the $\chi\bar{\chi}$ pair. The

Feynman diagrams of the 2-to-4 process for the EFT operators and for the light mediator models are shown in Fig. (8).

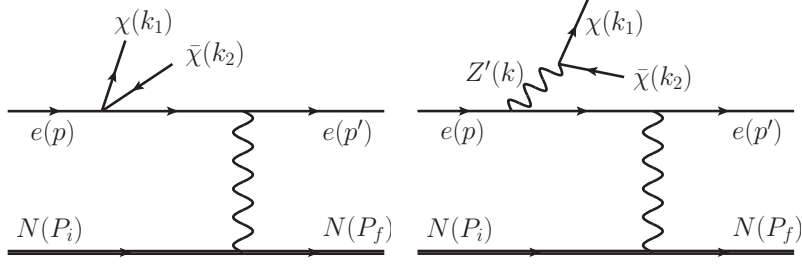


Figure 8. Diagrams for the DM 2-to-4 production processes at NA64 for the EFT operators (left) and for the light mediator models (right). Only the initial state radiation processes are shown here. DM can also be radiated from the final state electron.

The differential cross section of the 2-to-4 process is computed by

$$d\sigma(eN \rightarrow eN\chi\bar{\chi}) = \frac{1}{4E_e E_N v_{\text{rel}}} |\overline{\mathcal{M}}|^2 d\Phi^{(4)}, \quad (7.2)$$

where E_e (E_N) is the energy of the initial state electron (nucleus), v_{rel} is the relative velocity of the initial state electron and the initial state nucleus, $d\Phi^{(4)}$ is the four-body phase space for p' , P_f , k_1 , and k_2 , and $|\overline{\mathcal{M}}|^2$ is the usual matrix element square summed over final spins and averaged over initial spins. To compute the cross section of the 2-to-4 process, we decompose the 4-body phase space into a 2-body phase space (for $\chi\bar{\chi}$) and a 3-body phase space as follows,

$$d\Phi^{(4)}(P_f, p', k_1, k_2) = \frac{dk^2}{2\pi} d\Phi^{(3)}(P_f, p', k) \times d\Phi^{(2)}(k_1, k_2), \quad (7.3)$$

where $k = k_1 + k_2$. The matrix element of the 2-to-4 process can also be decomposed as follows

$$\mathcal{M} = \sum_i \mathcal{M}_{i,A}(p, p', P_i, P_f, k) \times J_i^A(k_1, k_2), \quad (7.4)$$

where

$$J_i^A(k_1, k_2) \equiv \bar{u}(k_1) \Gamma_i^A v(k_2), \quad (7.5)$$

with $\Gamma_i^A = \{1, \gamma^5, \gamma^\mu, \gamma^\mu \gamma^5, \sigma^{\mu\nu} / \sqrt{2}\}$ and $\sigma^{\mu\nu} = \frac{i}{2} [\gamma^\mu, \gamma^\nu]$. Here i denotes the interaction type, and A denotes the corresponding Lorentz indices. Therefore, $J_i^A(k_1, k_2)$ are J_1^A , J_3^A , and J_4^A for O_s , O_V , and O_A respectively. For the O_t operators, one can use the Fierz identity to re-arrange the fermionic fields as follows

$$\bar{\chi} \ell \bar{\ell} \chi = \sum_{i=1}^5 \lambda_i \bar{\ell} \Gamma_i \ell \bar{\chi} \Gamma_i \chi, \quad (7.6)$$

where $\lambda_i = \frac{1}{4} \{1, 1, 1, -1, 1\}$. Thus, all the five J_i^A 's are needed for the O_t case. We first integrate out the 2-body phase space

$$\chi_{ij}^{AB}(k) \equiv \int d\Phi^{(2)} \sum_{s_\chi, s_{\bar{\chi}}} J_i^A(J_j^B)^\dagger. \quad (7.7)$$

The expressions of the various χ_{ij}^{AB} 's are given in Appendix A.

Thus, the differential cross section of the 2-to-4 process is given by

$$d\sigma(eN \rightarrow eN\chi\bar{\chi}) = \frac{dk^2}{2\pi} \frac{\chi_{ij}^{AB}(k)}{k^4} \left[k^4 d\Phi^{(3)} \frac{\overline{\mathcal{M}_{i,A}\mathcal{M}_{j,B}^\dagger}}{4E_e E_N v_{\text{rel}}} \right] \equiv \frac{dk^2}{2\pi} \frac{\chi_{ij}^{AB}(k)}{k^4} \times d\sigma_{ij,AB}, \quad (7.8)$$

where the sum with repeated indices i and j is implicit, and $d\sigma_{ij}^{AB}$ is defined in such a way that it has the dimension of cross section. To compute $d\sigma_{ij}^{AB}$, we use the WWA [67, 68], in which the photon vertex with the lead nucleus can be replaced by an effective photon flux function. Thus, in the lab frame, one has [87]

$$\frac{d\sigma_{ij,AB}}{dx} \simeq k^4 \frac{\alpha\zeta}{16\pi^2} (1-x)\beta_k \int_{\tilde{u}_{\min}}^{\tilde{u}_{\max}} \frac{d\tilde{u}}{\tilde{u}^2} \overline{\tilde{\mathcal{M}}_{i,A}\tilde{\mathcal{M}}_{j,B}^\dagger} \Big|_{t=t_{\min}}, \quad (7.9)$$

where ζ is the photon flux, $x = k^0/E_e$, $\beta_k = \sqrt{1 - k^2/(xE_e)^2}$, $t = -(P_f - P_i)^2 = -q^2$, $t_{\min} = (k^2/2E_e)^2$, $\tilde{u}(\theta_k) = -E_e^2\theta_k^2 x - k^2(1-x)/x - m_e^2 x$, with θ_k being the polar angle of momentum k , $\tilde{u}_{\max} = \tilde{u}(\theta_k = 0)$, and $\tilde{u}_{\min} = \tilde{u}(\theta_k = \pi)$.¹² The matrix element $\tilde{\mathcal{M}}_{i,A}$ in Eq. 7.9 corresponds to the diagram that is obtained by removing the N particles both in the initial state and in final state (as well as the γNN vertex) in the diagram of $\mathcal{M}_{i,A}$. For illustration purposes, we also draw the diagrams for the process of $\tilde{\mathcal{M}}_{i,A}$ in Fig. 9, by introducing an imaginary particle V^A with the momentum k . However, the calculations of the cross section can be carried out without introducing the imaginary V^A particle. The expressions of the integrand in Eq. (7.9) contracted with χ_{ij}^{AB} for various models are given in Appendix A.

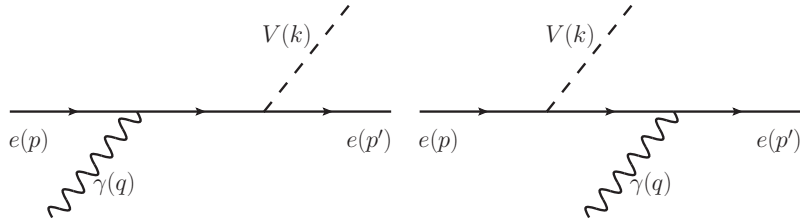


Figure 9. Feynman diagrams of $e^-(p) + \gamma(q) \rightarrow e^-(p') + V(k)$, where $V(k)$ represents the imaginary particle with momentum k , which carries the (multiple) Lorentz indices A . Note that because the matrix element $\tilde{\mathcal{M}}_{i,A}$ (as well as $\mathcal{M}_{i,A}$) contains the explicit Lorentz indices A , the corresponding “polarization vectors” of V are not included in the calculations of $\tilde{\mathcal{M}}_{i,A}$.

The effective photon flux ζ is given by [87, 88]

$$\zeta = \int_{t_{\min}}^{t_{\max}} dt \frac{t - t_{\min}}{t^2} G_2^{\text{el}}(t) = \int_{t_{\min}}^{t_{\max}} dt \frac{t - t_{\min}}{t^2} \left[\frac{Za^2 t}{(1 + a^2 t)(1 + t/d)} \right]^2, \quad (7.10)$$

¹²The limits \tilde{u}_{\min} and \tilde{u}_{\max} are determined by the range of θ_k . Because the missing energy signature includes dark matter emissions with arbitrary θ_k , one has $\tilde{u}_{\max} = \tilde{u}(\theta_k = 0)$ and $\tilde{u}_{\min} = \tilde{u}(\theta_k = \pi)$. We note that the usual approximation $\tilde{u}_{\min} \rightarrow -\infty$ [87] can fail for some cases; see appendix A for more detailed discussions.

where $t_{\max} = k^2 + m_e^2$, $G_2^{\text{el}}(t)$ is the elastic form-factor of the lead nucleus,¹³ $a = 111m_e^{-1}Z^{-1/3}$, $d = 0.164A^{-2/3} \text{ GeV}^2$, and we use $Z = 82$ and $A = 207.2$ for Pb.

Thus, the signal cross section as a function of the missing energy is given by

$$\frac{d\sigma}{dx}(eN \rightarrow eN\chi\bar{\chi}) = \int_{4m_\chi^2}^{x^2 E_e^2} dk^2 \left[\frac{\chi_{ij}^{AB}(k)}{2\pi k^4} \frac{d\sigma_{ij,AB}}{dx} \right] \equiv \int_{4m_\chi^2}^{x^2 E_e^2} dk^2 \frac{d\sigma}{dx dk^2}. \quad (7.11)$$

The expressions of $d\sigma/dxdk^2$ for various models are given in Appendix A. The signal region used by the NA64 collaboration is $E_{\text{miss}} > 0.5E_e$ [62], where E_e is the energy of electron beam and E_{miss} is the missing energy. Thus, the number of the signal events is computed via

$$N_s = N_{\text{EOT}} \times \frac{\rho_N}{m_N} \times L_{\text{eff}} \times \epsilon_d \times \int_{x_{\min}}^{1 - \frac{m_e}{E_e}} dx \frac{d\sigma}{dx}(eN \rightarrow eN\chi\bar{\chi}), \quad (7.12)$$

where $x_{\min} = 0.5$, $N_{\text{EOT}} = 2.84 \times 10^{11}$ is the total number of electron on target, $\rho_N = 11.34 \text{ g/cm}^3$ is the mass density of lead, $m_N = Am_p$ is the mass of the lead nucleus with $A = 207.2$ and $m_p \simeq 0.93 \text{ GeV}$, $\epsilon_d \simeq 0.5$ is the detection efficiency [62], L_{eff} is the effective length of the lead target for electron collision. We use the radiation length as the effective length, namely $L_{\text{eff}} \simeq X_0^{(e)} \simeq 0.5 \text{ cm}$, since the lead target in NA64 is a thick target for electrons [64]. We then compute the 90% C.L. limits on the light mediator models and EFT operators by using the criterion $N_s = 2.3$ based on the null background assumption [63].

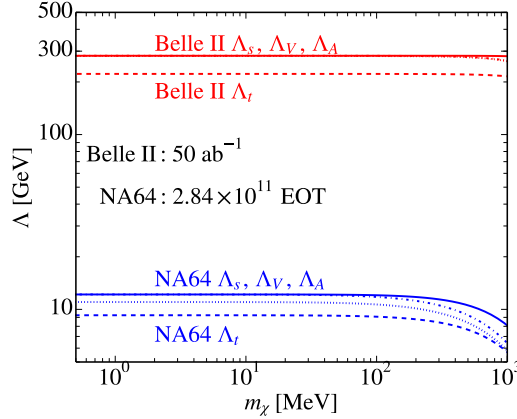


Figure 10. NA64 90% C.L. upper bound on the EFT operators: Λ_A (dot-dashed), Λ_V (solid), Λ_s (dotted), and Λ_t (dashed). The Belle II sensitivities are the same as Fig. 1.

The constraints on EFT operators are shown in Fig. 10. The NA64 constraints with the current EOT data on various Λ 's are about one order of magnitude smaller than the Belle II expected limits with 50 ab^{-1} data. The constraints on the light mediators with only vector or axial-vector couplings are shown in Fig. 11. For the three different $m_{Z'}$ cases, the NA64 constraints with the current EOT data are weaker than the Belle II expected limits with 50 ab^{-1} data, except the parameter space where $m_{Z'} = 10 \text{ MeV}$ and $m_{Z'} > 2m_\chi$.

¹³We neglect the inelastic form factor, which is usually much smaller than the elastic form factor for high Z targets [88].

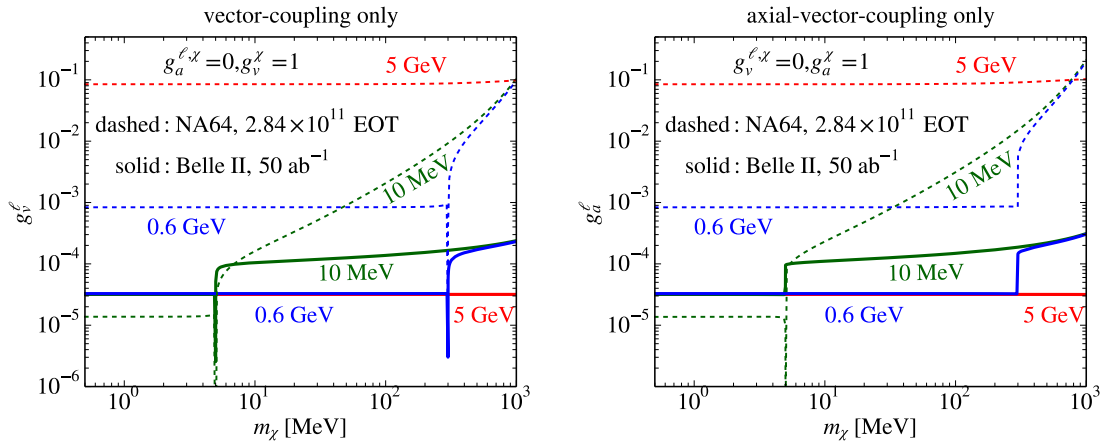


Figure 11. NA64 90% C.L. upper bond (dashed lines) on the light mediator models with vector couplings (left) and axial-vector couplings (right). The green, blue, and red lines show the constraints for $m_{Z'} = 10$ MeV, 0.6 GeV, and 5 GeV respectively. The Belle II sensitivities (solid lines) are the same as Fig. 2 and Fig. 3.

8 Dark matter relic density

In this section, we compare the parameter space of the DM operators/models in which the DM relic density (RD) is generated by the thermal freeze out mechanism, with that probed by the Belle II experiment. We compute the thermally averaged DM annihilation cross section $\langle\sigma_{\text{ann}}v_{\text{rel}}\rangle$ via [89]

$$\langle\sigma_{\text{ann}}v_{\text{rel}}\rangle = \frac{1}{8m_\chi^4 T_F K_2^2(m_\chi/T_F)} \int_{4m_\chi^2}^{\infty} ds \sigma_{\text{ann}} K_1\left(\frac{\sqrt{s}}{T_F}\right) (s - 4m_\chi^2) \sqrt{s}, \quad (8.1)$$

where σ_{ann} is the total DM annihilation cross section as a function of s , T is the temperature, and K_i are the modified Bessel functions of order i . For the EFT operators, the total DM annihilation cross section is $\sigma_{\text{ann}} = \sum_\ell \sigma(\bar{\chi}\chi \rightarrow \ell^+\ell^-)$; for the light mediator models, the total DM annihilation cross section is $\sigma_{\text{ann}} = \sigma(\bar{\chi}\chi \rightarrow Z'Z') + \sum_\ell \sigma(\bar{\chi}\chi \rightarrow \ell^+\ell^-)$, if kinematically allowed. The DM annihilation cross sections for various EFT operators and light mediator models are given in Appendix F. We solve the freeze-out temperature T_F via [90–92]

$$e^{x_F} = \sqrt{\frac{45}{8}} \frac{g_\chi m_\chi M_{\text{Pl}} c(c+2) \langle\sigma_{\text{ann}}v_{\text{rel}}\rangle}{2\pi^3 \sqrt{g_*} \sqrt{x_F}}, \quad (8.2)$$

where $x_F = m_\chi/T_F$, g_χ is the degrees of freedom of the DM, $c = 1/2$ is a matching constant, M_{Pl} is the Planck mass, g_* is the relativistic degrees of freedom in the thermal bath [93].

Fig. (12) shows the Belle II sensitivities (from the mono-photon channel) and NA64 constraints on the thermally averaged DM annihilation cross section $\langle\sigma_{\text{ann}}v_{\text{rel}}\rangle$ evaluated at the freeze-out temperature T_F , for the four EFT operators and for two light mediator models. The canonical thermal cross section ($\simeq 6 \times 10^{-26}$ cm³/s for Dirac DM [93]) in the mass range $m_\chi \lesssim$ GeV can be probed by Belle II with 50 ab⁻¹ for all the four EFT operators. For the two light vector mediator models with $m_{Z'} = 0.6$ GeV, the canonical

thermal cross section in the mass range $m_\chi \lesssim 0.2$ GeV can be probed by Belle II with 50 ab^{-1} . We also find that the 2.84×10^{11} EOT data accumulated at NA64 have already probed the canonical DM annihilation cross section with $m_\chi \lesssim 0.02$ GeV for the EFT operators, and with $m_\chi \lesssim 0.04$ GeV for the two light vector mediator models with $m_{Z'} = 0.6$ GeV.

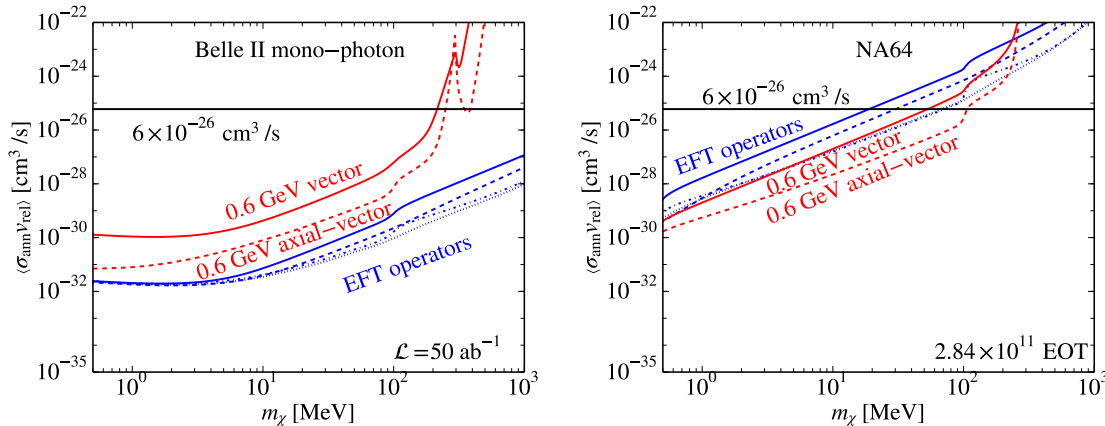


Figure 12. Left panel: Belle II 90% C.L. upper bound from the mono-photon channel with 50 ab^{-1} data on the thermally averaged DM annihilation cross section $\langle \sigma_{v_{\text{rel}}} \rangle$ evaluated at the freeze-out temperature. The blue lines correspond to the limits in Fig. (1) on EFT operators: O_A (dot-dashed), O_V (solid), O_s (dotted), and O_t (dashed). The red solid and dashed lines correspond to the $m_{Z'} = 0.6$ GeV models in Fig. (2) and (3) respectively. Right panel: NA64 90% C.L. upper bound with 2.84×10^{11} EOT data on the thermally averaged DM annihilation cross section evaluated at the freeze-out temperature. The blue lines correspond to the limits in Fig. (10) on EFT operators. The red solid (dashed) lines correspond to the $m_{Z'} = 0.6$ GeV vector-only (axial-vector-only) model in Fig. (11). The black solid line indicates the thermal cross section for the Dirac DM, $6 \times 10^{-26} \text{ cm}^3/\text{s}$ [93].

9 Summary

We investigate the capability of the Belle II and the NA64 experiments in probing the parameter space of the DM models in which DM only interacts with charged leptons in the SM. Our analyses focus on the sub-GeV Dirac DM, which is less constrained than WIMPs by the current DMDD experiments. We consider two different mechanisms to mediate the interactions between DM and charged leptons: EFT operators and light vector mediators in the MeV-GeV scale.

We compute the Belle II sensitivities in the mono-photon channel on the EFT operators. Our analysis shows that $\Lambda_t \lesssim 220$ GeV can be probed by Belle II with 50 ab^{-1} data, and $\Lambda \lesssim 280$ GeV can be probed for Λ_V , Λ_A and Λ_s . We find that the expected Belle II limits with 50 ab^{-1} data on EFT operators are of similar size to the LEP limits. The Belle II and LEP limits for sub-GeV DM can be several orders of magnitude stronger than the current DMDD limits, as well as the white dwarf limit.

The light mediator models can be searched for both in the mono-photon channel and in the di-muon channel at Belle II. We compute the Belle II sensitivities from both channels on

the light mediator models. The Belle II mono-photon sensitivities are analyzed for $m_{Z'} = 10$ MeV, 0.6 GeV and 5 GeV. The gauge coupling $g^\ell \simeq 3 \times 10^{-5}$ (both vector and axial-vector) can be probed by the Belle II mono-photon data, when $m_\chi < m_{Z'}/2$ and $g^\chi = 1$. The dimuon channel is complementary to the mono-photon channel and sometimes can be much better, for example in the parameter where $m_\chi > m_{Z'}/2$. Unlike the EFT operators, the Belle II sensitivities on the light mediator models (for example the $m_{Z'} \lesssim 5$ GeV model) can be several orders of magnitude stronger than the LEP limits, in the mono-photon channel. We also find that the collider limits have a rather weak dependence on the mediator mass; the DMDD cross section, however, is inversely proportional to $m_{Z'}^4$, thus leading to vastly different DM-electron interaction cross sections over more than 10 orders of magnitude in the parameter space considered in this study.

We also find that the Belle II mono-photon channel can probe the canonical DM thermal annihilation cross section for the DM mass \lesssim GeV for the EFT operators and ~ 0.2 GeV for the light mediator models considered. For both the EFT operators and the light mediator models, the Belle II sensitivities can be well below the “neutrino floor” expected in silicon detectors in DMDD. Thus the Belle II collider can probe the parameter space which is beyond the capability of current DMDD experiments, unless the neutrino floor can be mitigated in a satisfactory way.

We compute the NA64 constraints (with 2.84×10^{11} EOT data) both on the EFT operators and on the light vector mediator models. We find that the NA64 can probe interesting parameter space of DM models. For the EFT operators, the NA64 upper bound on the new physics scales Λ are typically smaller than the Belle II sensitivities. However, for the light mediator models (for example, the $m_{Z'} = 10$ MeV model with $m_\chi < m_{Z'}/2$), NA64 can probe the parameter space that is beyond the capability of Belle II. Thus, the NA64 and Belle II experiments can be complementary in probing sub-GeV DM models. The analytic expressions of the DM production cross section at the NA64 for the EFT operators and the vector mediator models are provided in the appendix.

10 Acknowledgement

We thank Yong-Heng Xu, Li-Gang Xia, and Sandra Robles for helpful discussions. The work is supported in part by the National Natural Science Foundation of China under Grant No. 11775109.

A DM production cross sections at NA64

We provide the results of the 2-body phase space integral for the DM currents and the DM production cross sections at NA64 in the WWA in this appendix. The tensor χ_{ij}^{AB} for the DM currents can be parameterized as follows

$$\chi_{ij}^{AB} = \sum_{\text{spins}} \int d\Phi^{(2)} [\bar{u}(k_1)\Gamma_i^A v(k_2)] [\bar{u}(k_1)\Gamma_j^B v(k_2)]^\dagger \equiv \frac{1}{12\pi} \beta_\chi T_{ij}^{AB}, \quad (\text{A.1})$$

where $\beta_\chi = \sqrt{1 - 4m_\chi^2/k^2}$, and $\Gamma_i^A = \{1, \gamma^5, \gamma^\mu, \gamma^\mu \gamma^5, \sigma^{\mu\nu}/\sqrt{2}\}$ with $\sigma^{\mu\nu} = \frac{i}{2}[\gamma^\mu, \gamma^\nu]$.¹⁴ The various two-body phase space integrals in Eq. (A.1) can be simplified by the following relations

$$\int d\Phi^{(2)} F(k_1, k_2) = \frac{\beta_\chi}{96\pi} I(k). \quad (\text{A.2})$$

We have $I(k) = 12$ for $F(k_1, k_2) = 1$; $I(k) = 6k^\mu$ for $F(k_1, k_2) = k_1^\mu$ or k_2^μ ; and $I(k) = k^2 \beta_\chi^2 g^{\mu\nu} + (3 - \beta_\chi^2) k^\mu k^\nu$ for $F(k_1, k_2) = k_1^\mu k_2^\nu$ or $k_2^\mu k_1^\nu$. Because $(\chi_{ij}^{AB})^\dagger = \chi_{ji}^{BA}$, we have $(T_{ij}^{AB})^\dagger = T_{ji}^{BA}$. The non-zero independent T_{ij}^{AB} 's are

$$T_{11}^{AB} = 3k^2 \beta_\chi^2, \quad (\text{A.3})$$

$$T_{22}^{AB} = 3k^2, \quad (\text{A.4})$$

$$T_{33}^{AB} = (3 - \beta_\chi^2)(k^\mu k^\rho - g^{\mu\rho} k^2), \quad (\text{A.5})$$

$$T_{44}^{AB} = (3 - \beta_\chi^2) k^\mu k^\rho - 2g^{\mu\rho} k^2 \beta_\chi^2, \quad (\text{A.6})$$

$$T_{55}^{AB} = \frac{(3 - \beta_\chi^2)}{2} (g^{\mu\sigma} k^\nu k^\rho - g^{\mu\rho} k^\sigma k^\nu + g^{\nu\rho} k^\mu k^\sigma - g^{\nu\sigma} k^\mu k^\rho) - \frac{k^2 \beta_\chi^2}{2} (g^{\mu\sigma} g^{\nu\rho} - g^{\nu\sigma} g^{\mu\rho}), \quad (\text{A.7})$$

$$T_{24}^{AB} = 3\sqrt{k^2(1 - \beta_\chi^2)} k^\rho, \quad (\text{A.8})$$

$$T_{35}^{AB} = \frac{3i}{\sqrt{2}} \sqrt{k^2(1 - \beta_\chi^2)} (k^\rho g^{\sigma\mu} - k^\sigma g^{\rho\mu}), \quad (\text{A.9})$$

where we have always used Lorentz indices “ $\mu\nu$ ” for “ A ” and “ $\rho\sigma$ ” for “ B ”. The χ_{ij}^{AB} of O_s , O_V , and O_A , are χ_{11}^{AB} , χ_{33}^{AB} , and χ_{44}^{AB} respectively. The χ_{ij}^{AB} for the light mediator model with the vector (axial-vector) couplings is χ_{33}^{AB} (χ_{44}^{AB}). For the O_t operator, one has to consider all the χ_{ij}^{AB} 's combined with the coefficients in the Fierz transformation.

The DM differential cross section in NA64 can be computed in WWA. The relevant integrand in Eq. (7.9) contracted with χ_{ij}^{AB} for the EFT operators can be parameterized as

$$\frac{1}{\tilde{u}^2} \sum_{i,j} \chi_{ij}^{AB} \overline{\tilde{\mathcal{M}}_{i,A}} \tilde{\mathcal{M}}_{j,B}^\dagger \Big|_{t=t_{\min}} = \frac{e^2 \beta_\chi}{6\pi \Lambda^4} \sum_{n=1,2,3,4} \frac{C_n}{\tilde{u}^n} \quad (\text{A.10})$$

We have $C_1 = 0$ for the O_V , O_A , and O_s cases. The C_i ($i = 2, 3, 4$) for O_V are

$$C_2 = -\frac{2(k^2 + 2m_\chi^2)(x^2 - 2x + 2)}{(x - 1)}, \quad (\text{A.11})$$

$$C_3 = 4x(k^2 + 2m_\chi^2)(2m_e^2 + k^2), \quad (\text{A.12})$$

$$C_4 = -4(k^2 + 2m_\chi^2)(2m_e^2 + k^2)(k^2(x - 1) - x^2 m_e^2). \quad (\text{A.13})$$

The C_i ($i = 2, 3, 4$) for O_A are

$$C_2 = -\frac{4x^2 m_e^2 (k^2 + 2m_\chi^2) + 2k^2 (x^2 - 2x + 2) (k^2 - 4m_\chi^2)}{k^2(x - 1)}, \quad (\text{A.14})$$

$$C_3 = 4x(-4m_e^2(k^2 - 7m_\chi^2) + k^4 - 4k^2 m_\chi^2), \quad (\text{A.15})$$

$$C_4 = -4(-4m_e^2(k^2 - 7m_\chi^2) + k^4 - 4k^2 m_\chi^2)(k^2(x - 1) - x^2 m_e^2). \quad (\text{A.16})$$

¹⁴Note that there is no explicit Lorentz index for $\{1, \gamma^5\}$; $A = \mu$ for $\{\gamma^\mu, \gamma^\mu \gamma^5\}$; $A = \mu\nu$ for $\sigma^{\mu\nu}/\sqrt{2}$.

The C_i ($i = 2, 3, 4$) for O_s are

$$C_2 = -\frac{3x^2(k^2 - 4m_\chi^2)}{2(x-1)}, \quad (\text{A.17})$$

$$C_3 = 3x(k^2 - 4m_\chi^2)(k^2 - 4m_e^2), \quad (\text{A.18})$$

$$C_4 = -3(k^2 - 4m_\chi^2)(k^2 - 4m_e^2)(k^2(x-1) - x^2m_e^2). \quad (\text{A.19})$$

The C_i ($i = 1, 2, 3, 4$) for O_t are

$$C_1 = \frac{x(2m_\chi^2 + k^2)}{4k^2(x-1)}, \quad (\text{A.20})$$

$$C_2 = \frac{-1}{4k^2(x-1)} [6k^2x^2m_em_\chi + x^2m_e^2(k^2 + 2m_\chi^2) + 2k^2(x^2 - x + 1)(k^2 - m_\chi^2)], \quad (\text{A.21})$$

$$C_3 = x(6k^2m_em_\chi - m_e^2(k^2 - 16m_\chi^2) + k^4 - k^2m_\chi^2), \quad (\text{A.22})$$

$$C_4 = -(6k^2m_em_\chi - m_e^2(k^2 - 16m_\chi^2) + k^4 - k^2m_\chi^2)(k^2(x-1) - x^2m_e^2). \quad (\text{A.23})$$

Therefore, the differential DM production cross section at NA64 in the WWA (defined in Eq. (7.11)) can be written as

$$\frac{d\sigma(eN \rightarrow eN\bar{\chi}\chi)}{dxdk^2} = \frac{\alpha^2\zeta(1-x)\beta_k\beta_\chi}{48\pi^3\Lambda^4} \left[C_1 \ln(\tilde{u}) - \sum_{n=2,3,4} \frac{C_n}{(n-1)\tilde{u}^{n-1}} \right] \Big|_{\tilde{u}_{\min}}^{\tilde{u}_{\max}}. \quad (\text{A.24})$$

Because the cross section is usually dominated by the small angle emissions $\theta_k \ll 1$, one can use the approximation $\tilde{u}_{\min} \rightarrow -\infty$ to further simplify the expressions [87] if $C_1 = 0$. For the light mediators with vector and axial-vector couplings, one just needs to make the following replacement

$$\frac{1}{\Lambda^4} \rightarrow \frac{g_\ell^2 g_\chi^2}{(k^2 - m_{Z'}^2)^2 + m_{Z'}^2 \Gamma_{Z'}^2}. \quad (\text{A.25})$$

B Mono-photon cross sections of the EFT operators at Belle II

The differential cross section of $e^+e^- \rightarrow \chi\bar{\chi}\gamma$ for the four EFT operators in our analysis have been computed in Ref. [46]. Here we collect the expressions of the cross section for the $e^+e^- \rightarrow \chi\bar{\chi}\gamma$ process given in Ref. [46]. For the vector case, the cross section is

$$\frac{d\sigma}{dE_\gamma d\cos\theta_\gamma} = \frac{\alpha\sqrt{s}}{12\pi^2\Lambda_V^4} \frac{(1-z+2\mu^2)}{z\sin^2\theta_\gamma} \sqrt{\frac{1-z-4\mu^2}{1-z}} [(z-2)^2 + z^2\cos^2\theta_\gamma]. \quad (\text{B.1})$$

For the axial-vector case, the cross section is

$$\frac{d\sigma}{dE_\gamma d\cos\theta_\gamma} = \frac{\alpha\sqrt{s}}{12\pi^2\Lambda_A^4} \frac{(1-z)}{z\sin^2\theta_\gamma} \left(\frac{1-z-4\mu^2}{1-z} \right)^{3/2} [(z-2)^2 + z^2\cos^2\theta_\gamma]. \quad (\text{B.2})$$

For the ‘‘s-channel’’ scalar case, the cross section is

$$\frac{d\sigma}{dE_\gamma d\cos\theta_\gamma} = \frac{\alpha\sqrt{s}}{8\pi^2\Lambda_s^4} \frac{(1-z)}{z\sin^2\theta_\gamma} \left(\frac{1-z-4\mu^2}{1-z} \right)^{3/2} [2(1-z) + z^2]. \quad (\text{B.3})$$

For the “t-channel” scalar case, the cross section is

$$\frac{d\sigma}{dE_\gamma d\cos\theta_\gamma} = \frac{\alpha\sqrt{s}}{192\pi^2\Lambda_t^4} \frac{1}{z\sin^2\theta_\gamma} \sqrt{\frac{1-z-4\mu^2}{1-z}} \left[\left(2-z + \frac{2\mu^2 z}{1-z} \right) (3z^2 - 6z + 4) - 8\mu^2 \right. \\ \left. + (1-z+2\mu^2) \left(2(z-2)^2 + \left(2z^2 - \frac{1}{1-z} \right) \cos^2\theta_\gamma \right) \right]. \quad (\text{B.4})$$

Here E_γ and θ_γ are the energy and the polar angle (with respect to the direction of the initial electron) of the final state photon in the CM frame, s is the square of the center of mass energy, m_χ is the mass of the dark matter, $z = 2E_\gamma/\sqrt{s}$, and $\mu = m_\chi/\sqrt{s}$.

C Matrix elements for EFT operators in DMDD

The matrix elements of the four EFT operators, given in Eqs. (2.1, 2.2, 2.3, 2.4), in the DMDD experiments are given by

$$\Lambda_s^4 \overline{|\mathcal{M}_{\chi e}|^2} = (t - 4m_e^2)(t - 4m_\chi^2), \quad (\text{C.1})$$

$$\Lambda_t^4 \overline{|\mathcal{M}_{\chi e}|^2} = ((m_e - m_\chi)^2 - s)^2, \quad (\text{C.2})$$

$$\Lambda_V^4 \overline{|\mathcal{M}_{\chi e}|^2} = 4(m_e^2 + m_\chi^2 - s)^2 + 4st + 2t^2, \quad (\text{C.3})$$

$$\Lambda_A^4 \overline{|\mathcal{M}_{\chi e}|^2} = 2(2m_e^4 + 4m_e^2(5m_\chi^2 - s - t) + 2m_\chi^4 - 4m_\chi^2(s + t) + 2s^2 + 2st + t^2), \quad (\text{C.4})$$

where s and t are Mandelstam variables. For the non-relativistic dark matter, one has $s \simeq (m_e + m_\chi)^2$ and $t \simeq -q^2$. The typical momentum transfer in the DM-electron scattering is $q_{\text{typ}} \sim Z_{\text{eff}} \alpha m_e$, where $Z_{\text{eff}} = 12.4$ for the outermost shell electron of Xenon atom [77, 94, 95]. We display the q dependence of the form factor $F_{\text{DM}}(q)$ for all the four EFT operators considered, which shows that the deviation from $F_{\text{DM}}(q) = 1$ is less than 0.5% in the range of $q \lesssim Z_{\text{eff}} \alpha m_e$ for all the EFT operators. Thus, it is a good approximation to use $F_{\text{DM}}(q) = 1$ in the DMDD calculation for these EFT operators.

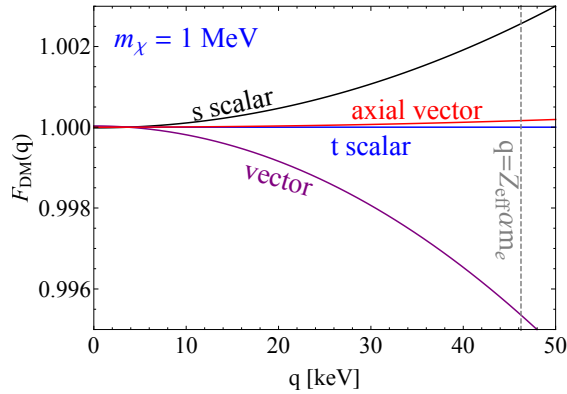


Figure 13. The form factor $F_{\text{DM}}(q)$ as a function of q for four EFT operators: vector (purple), axial-vector (red), s-channel scalar (black), and t-channel scalar (blue). The typical q range in DMDD with Xe target is $q \lesssim Z_{\text{eff}} \alpha m_e$ where $Z_{\text{eff}} = 12.4$. We use $m_\chi = 1$ MeV here.

D LEP analysis

In this section, we describe our LEP analysis, which closely follows the analysis in Ref. [39]. To properly take into account the initial state radiation effect, we use CALCHEP [96] to generate 10^5 events for each model point for the process of $e^+e^- \rightarrow \chi\bar{\chi}\gamma$ at $\sqrt{s} = 200$ GeV (with 100 GeV for each beam).¹⁵ The DELPHI detector has three main electromagnetic calorimeters: the Small angle Tile Calorimeter (STIC), the Forward ElectroMagnetic Calorimeter (FEMC), and the High density Projection Chamber (HPC). We smear the photon events by using the gaussian distributions with the energy resolutions given in Table 1. Following Ref. [39], an additional Lorentzian energy smearing

$$L(E) = \frac{1}{\pi} \frac{\Gamma/2}{(E - E_\gamma)^2 + (\Gamma/2)^2}, \quad (\text{D.1})$$

where $\Gamma = 0.052E_\gamma$ is further performed. We analyzed the events with the preselection cuts shown in Table 1.

	$\sigma_{E_\gamma}/E_\gamma$	Preselection cuts
STIC	$0.0152 \oplus (0.135/\sqrt{E_\gamma})$	(i) $x_\gamma > 0.3$ (ii) $\theta_\gamma > 9.2^\circ - 9^\circ x_\gamma$ when $3.8^\circ < \theta < 8^\circ$ $180^\circ - \theta_\gamma > 9.2^\circ - 9^\circ x_\gamma$ when $172^\circ < \theta < 176.2^\circ$
FEMC	$0.03 \oplus (0.12/\sqrt{E_\gamma}) \oplus (0.11/E_\gamma)$	(i) $x_\gamma > 0.1$ (ii) $\theta_\gamma > 28^\circ - 80^\circ x_\gamma$ when $12^\circ < \theta < 32^\circ$ $180 - \theta_\gamma > 28^\circ - 80^\circ x_\gamma$ when $148^\circ < \theta < 168^\circ$
HPC	$0.043 \oplus (0.32/\sqrt{E_\gamma})$	(i) $x_\gamma > 0.06$ (ii) $45^\circ < \theta < 135^\circ$

Table 1. Preselection cuts and energy resolution for the three sub-detectors in the electromagnetic calorimeters in DELPHI: STIC, FEMC, and HPC [71]. Here E_γ is in unit of GeV, and $x_\gamma = E_\gamma/E_{\text{beam}}$.

We further take into account other efficiency factors beyond the detector cuts given in Table 1, as analyzed in Ref. [39]. They include the trigger efficiency, the analysis efficiency, and an overall factor of 90%, which is found to be necessary for the simulations in Ref. [39] to match the simulations in Ref. [71]. For HPC, the trigger efficiency is a linear interpolation function with 52% at $E_\gamma = 6$ GeV, 77% at $E_\gamma = 30$ GeV, and 84% at $E_\gamma = 100$ GeV; the analysis efficiency is a linear interpolation function with 41% at $E_\gamma = 6$ GeV and 78% at $E_\gamma > 80$ GeV [39]. For FEMC, the trigger efficiency is a linear interpolation function with 93% at $E_\gamma = 10$ GeV and 100% at $E_\gamma > 15$ GeV; the analysis efficiency is a linear interpolation function with 51% at $E_\gamma = 10$ GeV and 67% at $E_\gamma = 100$ GeV [39]. For STIC, the product of the trigger efficiency and the analysis efficiency is 48% for $E_\gamma > 30$ GeV. [39].

¹⁵Ref. [39] found that using $\sqrt{s} = 200$ GeV only introduces a small deviation from the full analysis.

We bin the data in 19 bins with $0.05 < x_\gamma < 1$, where $x_\gamma = E_\gamma/E_{\text{beam}}$ and compute the χ^2 via

$$\chi^2 = \sum_{i=1}^{19} \frac{(N_i^s + N_i^b - N_i^o)^2}{\sigma_i^2}, \quad (\text{D.2})$$

where N_i^s is the number of signal events, N_i^b is the number of background events, N_i^o is the number of observed data events, and σ_i is the uncertainty. Here the dominant background process is the $e^+e^- \rightarrow \nu\nu\gamma$ process. We take N_i^b , N_i^o , and σ_i from Refs. [39, 71]. The LEP limits at 90% CL on light mediator models are obtained by $\chi^2/\text{dof} = 27.2/19$.

E Confidence Level Limits

We provide the derivation for the two confidence level (denoted as C.L. or CL) limits used in our analysis which are based on a non-zero background and a null background respectively. The CL is usually defined via $\text{CL} = 1 - \alpha$ [97].

For the analysis with a non-zero background (e.g., the Belle II limits in our analysis), we assume a Gaussian distribution for the likelihood distribution $\mathcal{L}(N_s)$ for the signal events N_s as follows

$$\mathcal{L}(N_s) = \frac{1}{\sqrt{2\pi}\sigma} \exp\left(-\frac{N_s^2}{2\sigma^2}\right), \quad (\text{E.1})$$

where $\sigma = \sqrt{N_b}$ with N_b being the number of the background events. In this case, α is given by [97]

$$\frac{\alpha}{2} = \int_{N_s^{\text{up}}}^{+\infty} \mathcal{L}(N_s) dN_s, \quad (\text{E.2})$$

where N_s^{up} is the upper bound on the signal events N_s with the given confidence level. Therefore, the 90% CL limit in this case corresponds to $N_s^{\text{up}} \simeq \sqrt{2.71}\sqrt{N_b}$.

For the analysis with a null background (e.g., the NA64 limits in our analysis), we assume a Poisson distribution for $\mathcal{L}(N_s)$, which is

$$\mathcal{L}(N_s) = e^{-N_s}. \quad (\text{E.3})$$

In this case, α is given by [97]

$$\alpha = \int_{N_s^{\text{up}}}^{+\infty} \mathcal{L}(N_s) dN_s. \quad (\text{E.4})$$

Therefore, the 90% CL limit in this case corresponds to $N_s^{\text{up}} = 2.3$.

F DM annihilation cross sections

For the Z' model with only vector couplings, the DM annihilation cross sections are

$$\sigma(\chi\bar{\chi} \rightarrow \ell\ell) = \frac{(g_v^\ell g_v^\chi)^2 \beta_\ell (2m_\ell^2 + s) (2m_\chi^2 + s)}{12\pi s \beta_d (\beta_d^2 m_{Z'}^2 s + (m_{Z'}^2 - s)^2)}, \quad (\text{F.1})$$

$$\begin{aligned} \sigma(\chi\bar{\chi} \rightarrow Z'Z') &= \frac{(g_v^\chi)^4 \beta_{Z'}}{4\pi s \beta_d} \left(-\frac{(2m_\chi^2 + m_{Z'}^2)^2 + \beta_{Z'}^2 m_\chi^2 s + m_{Z'}^4}{\beta_{Z'}^2 m_\chi^2 s + m_{Z'}^4} \right. \\ &\quad \left. + \frac{2(4m_\chi^2 (s - 2m_{Z'}^2 - 2m_\chi^2) + 4m_{Z'}^4 + s^2)}{(s - 2m_{Z'}^2) \beta_{Z'} \beta_d s} \operatorname{arccoth} \left(\frac{s - 2m_{Z'}^2}{\beta_{Z'} \beta_d s} \right) \right), \quad (\text{F.2}) \end{aligned}$$

where m_ℓ is the lepton mass, and

$$\beta_\ell = \sqrt{1 - \frac{4m_\ell^2}{s}}, \quad \beta_d = \sqrt{1 - \frac{4m_\chi^2}{s}}, \quad \beta_{Z'} = \sqrt{1 - \frac{4m_{Z'}^2}{s}}. \quad (\text{F.3})$$

For the Z' model with only axial-vector couplings, the DM annihilation cross sections are

$$\sigma(\chi\bar{\chi} \rightarrow \ell\ell) = \frac{(g_a^\ell g_a^\chi)^2 \beta_\ell (-4s(m_\ell^2 + m_\chi^2) + 28m_\ell^2 m_\chi^2 + s^2)}{12\pi s \beta_d (\beta_d^2 m_{Z'}^2 s + (m_{Z'}^2 - s)^2)}, \quad (\text{F.4})$$

$$\begin{aligned} \sigma(\chi\bar{\chi} \rightarrow Z'Z') &= \frac{(g_a^\chi)^4 \beta_{Z'}}{4\pi s m_{Z'}^4 \beta_d} \left(2\beta_{Z'}^2 m_\chi^2 s - m_{Z'}^4 - \frac{m_{Z'}^4 (m_{Z'}^2 - 4m_\chi^2)^2}{\beta_{Z'}^2 m_\chi^2 s + m_{Z'}^4} \right. \\ &\quad \left. + \frac{2(m_{Z'}^4 (4m_{Z'}^4 + s^2) + 4\beta_{Z'}^2 m_\chi^2 s (s(m_{Z'}^2 - m_\chi^2) + m_{Z'}^4))}{(s - 2m_{Z'}^2) \beta_{Z'} \beta_d s} \operatorname{arccoth} \left(\frac{s - 2m_{Z'}^2}{\beta_{Z'} \beta_d s} \right) \right). \quad (\text{F.5}) \end{aligned}$$

The DM annihilation cross sections for the EFT operators are

$$\sigma_V(\chi\bar{\chi} \rightarrow \ell\ell) = \frac{\beta_\ell (2m_\ell^2 + s) (2m_\chi^2 + s)}{12\pi s \Lambda_V^4 \beta_d}, \quad (\text{F.6})$$

$$\sigma_A(\chi\bar{\chi} \rightarrow \ell\ell) = \frac{\beta_\ell (-4s(m_\ell^2 + m_\chi^2) + 28m_\ell^2 m_\chi^2 + s^2)}{12\pi \Lambda_A^4 s \beta_d}, \quad (\text{F.7})$$

$$\sigma_s(\chi\bar{\chi} \rightarrow \ell\ell) = \frac{\beta_\ell \beta_d s}{16\pi \Lambda_s^4}, \quad (\text{F.8})$$

$$\sigma_t(\chi\bar{\chi} \rightarrow \ell\ell) = \frac{\beta_\ell (-s(m_\ell^2 + 6m_\ell m_\chi + m_\chi^2) + 16m_\ell^2 m_\chi^2 + s^2)}{48\pi \Lambda_t^4 s \beta_d}. \quad (\text{F.9})$$

References

- [1] G. Bertone, D. Hooper, and J. Silk, ‘‘Particle dark matter: Evidence, candidates and constraints,’’ *Phys. Rept.* **405** (2005) 279–390 [[hep-ph/0404175](#)].
- [2] J. L. Feng, ‘‘Dark Matter Candidates from Particle Physics and Methods of Detection,’’ *Ann. Rev. Astron. Astrophys.* **48** (2010) 495–545 [[arXiv:1003.0904](#)].

- [3] L. Roszkowski, E. M. Sessolo, and S. Trojanowski, “WIMP dark matter candidates and searches—current status and future prospects,” *Rept. Prog. Phys.* **81** (2018) 066201 [[arXiv:1707.06277](#)].
- [4] M. Schumann, “Direct Detection of WIMP Dark Matter: Concepts and Status,” *J. Phys. G* **46** (2019) 103003 [[arXiv:1903.03026](#)].
- [5] R. Essig, T. Volansky, and T.-T. Yu, “New Constraints and Prospects for sub-GeV Dark Matter Scattering off Electrons in Xenon,” *Phys. Rev. D* **96** (2017) 043017 [[arXiv:1703.00910](#)].
- [6] **XENON** Collaboration, “Light Dark Matter Search with Ionization Signals in XENON1T,” *Phys. Rev. Lett.* **123** (2019) 251801 [[arXiv:1907.11485](#)].
- [7] **DarkSide** Collaboration, “Constraints on Sub-GeV Dark-Matter–Electron Scattering from the DarkSide-50 Experiment,” *Phys. Rev. Lett.* **121** (2018) 111303 [[arXiv:1802.06998](#)].
- [8] **PandaX-II** Collaboration, “Search for Light Dark Matter-Electron Scatterings in the PandaX-II Experiment,” *Phys. Rev. Lett.* **126** (2021) 211803 [[arXiv:2101.07479](#)].
- [9] **SENSEI** Collaboration, “SENSEI: Direct-Detection Results on sub-GeV Dark Matter from a New Skipper-CCD,” *Phys. Rev. Lett.* **125** (2020) 171802 [[arXiv:2004.11378](#)].
- [10] **DAMIC** Collaboration, “Constraints on Light Dark Matter Particles Interacting with Electrons from DAMIC at SNOLAB,” *Phys. Rev. Lett.* **123** (2019) 181802 [[arXiv:1907.12628](#)].
- [11] **EDELWEISS** Collaboration, “First germanium-based constraints on sub-MeV Dark Matter with the EDELWEISS experiment,” *Phys. Rev. Lett.* **125** (2020) 141301 [[arXiv:2003.01046](#)].
- [12] **SuperCDMS** Collaboration, “First Dark Matter Constraints from a SuperCDMS Single-Charge Sensitive Detector,” *Phys. Rev. Lett.* **121** (2018) 051301 [[arXiv:1804.10697](#)]. [Erratum: *Phys.Rev.Lett.* 122, 069901 (2019)].
- [13] N. F. Bell, G. Busoni, M. E. Ramirez-Quezada, S. Robles, and M. Virgato, “Improved treatment of dark matter capture in white dwarfs,” *JCAP* **10** (2021) 083 [[arXiv:2104.14367](#)].
- [14] G. Bertone and M. Fairbairn, “Compact Stars as Dark Matter Probes,” *Phys. Rev. D* **77** (2008) 043515 [[arXiv:0709.1485](#)].
- [15] M. McCullough and M. Fairbairn, “Capture of Inelastic Dark Matter in White Dwarves,” *Phys. Rev. D* **81** (2010) 083520 [[arXiv:1001.2737](#)].
- [16] D. Hooper, D. Spolyar, A. Vallinotto, and N. Y. Gnedin, “Inelastic Dark Matter As An Efficient Fuel For Compact Stars,” *Phys. Rev. D* **81** (2010) 103531 [[arXiv:1002.0005](#)].
- [17] P. Amaro-Seoane, J. Casanellas, R. Schödel, E. Davidson, and J. Cuadra, “Probing dark matter crests with white dwarfs and IMBHs,” *Mon. Not. Roy. Astron. Soc.* **459** (2016) 695–700 [[arXiv:1512.00456](#)].
- [18] G. Panotopoulos and I. Lopes, “Constraints on light dark matter particles using white dwarf stars,” *Int. J. Mod. Phys. D* **29** (2020) 2050058 [[arXiv:2005.11563](#)].
- [19] Y. Ema, F. Sala, and R. Sato, “Light Dark Matter at Neutrino Experiments,” *Phys. Rev. Lett.* **122** (2019) 181802 [[arXiv:1811.00520](#)].

- [20] J. B. Dent, B. Dutta, J. L. Newstead, I. M. Shoemaker, and N. T. Arellano, “Present and future status of light dark matter models from cosmic-ray electron upscattering,” *Phys. Rev. D* **103** (2021) 095015 [[arXiv:2010.09749](#)].
- [21] Q.-H. Cao, R. Ding, and Q.-F. Xiang, “Searching for sub-MeV boosted dark matter from xenon electron direct detection,” *Chin. Phys. C* **45** (2021) 045002 [[arXiv:2006.12767](#)].
- [22] H. An, M. Pospelov, J. Pradler, and A. Ritz, “Directly Detecting MeV-scale Dark Matter via Solar Reflection,” *Phys. Rev. Lett.* **120** (2018) 141801 [[arXiv:1708.03642](#)]. [Erratum: *Phys.Rev.Lett.* 121, 259903 (2018)].
- [23] T. Emken, “Solar reflection of light dark matter with heavy mediators.” [arXiv:2102.12483](#).
- [24] E. Kou and P. Urquijo, eds., “The Belle II Physics Book,” *PTEP* **2019** (2019) 123C01 [[arXiv:1808.10567](#)]. [Erratum: *PTEP* 2020, 029201 (2020)].
- [25] **BaBar** Collaboration, “The BaBar detector,” *Nucl. Instrum. Meth. A* **479** (2002) 1–116 [[hep-ex/0105044](#)].
- [26] J. Liang, Z. Liu, Y. Ma, and Y. Zhang, “Millicharged particles at electron colliders,” *Phys. Rev. D* **102** (2020) 015002 [[arXiv:1909.06847](#)].
- [27] M. Duerr, *et al.*, “Invisible and displaced dark matter signatures at Belle II,” *JHEP* **02** (2020) 039 [[arXiv:1911.03176](#)].
- [28] M. Duerr, T. Ferber, C. Garcia-Cely, C. Hearty, and K. Schmidt-Hoberg, “Long-lived Dark Higgs and Inelastic Dark Matter at Belle II,” *JHEP* **04** (2021) 146 [[arXiv:2012.08595](#)].
- [29] D. W. Kang, P. Ko, and C.-T. Lu, “Exploring properties of long-lived particles in inelastic dark matter models at Belle II,” *JHEP* **04** (2021) 269 [[arXiv:2101.02503](#)].
- [30] R. Essig, J. Mardon, M. Papucci, T. Volansky, and Y.-M. Zhong, “Constraining Light Dark Matter with Low-Energy e^+e^- Colliders,” *JHEP* **11** (2013) 167 [[arXiv:1309.5084](#)].
- [31] E. Izaguirre, G. Krnjaic, and B. Shuve, “Discovering Inelastic Thermal-Relic Dark Matter at Colliders,” *Phys. Rev. D* **93** (2016) 063523 [[arXiv:1508.03050](#)].
- [32] A. Filimonova, R. Schäfer, and S. Westhoff, “Probing dark sectors with long-lived particles at BELLE II,” *Phys. Rev. D* **101** (2020) 095006 [[arXiv:1911.03490](#)].
- [33] E. Izaguirre, G. Krnjaic, P. Schuster, and N. Toro, “Analyzing the Discovery Potential for Light Dark Matter,” *Phys. Rev. Lett.* **115** (2015) 251301 [[arXiv:1505.00011](#)].
- [34] C. Boehm, X. Chu, J.-L. Kuo, and J. Pradler, “Scalar dark matter candidates revisited,” *Phys. Rev. D* **103** (2021) 075005 [[arXiv:2010.02954](#)].
- [35] J. R. Ellis, J. L. Feng, A. Ferstl, K. T. Matchev, and K. A. Olive, “Prospects for detecting supersymmetric dark matter at post LEP benchmark points,” *Eur. Phys. J. C* **24** (2002) 311–322 [[astro-ph/0110225](#)].
- [36] A. Freitas and S. Westhoff, “Leptophilic Dark Matter in Lepton Interactions at LEP and ILC,” *JHEP* **10** (2014) 116 [[arXiv:1408.1959](#)].
- [37] R. Primulando, J. Julio, and P. Uttayarat, “Collider Constraints on a Dark Matter Interpretation of the XENON1T Excess,” *Eur. Phys. J. C* **80** (2020) 1084 [[arXiv:2006.13161](#)].
- [38] F. Richard, G. Arcadi, and Y. Mambrini, “Searching for dark matter at colliders,” *Eur. Phys. J. C* **75** (2015) 171 [[arXiv:1411.0088](#)].

- [39] P. J. Fox, R. Harnik, J. Kopp, and Y. Tsai, “LEP Shines Light on Dark Matter,” *Phys. Rev. D* **84** (2011) 014028 [[arXiv:1103.0240](#)].
- [40] R. Essig, P. Schuster, and N. Toro, “Probing Dark Forces and Light Hidden Sectors at Low-Energy e^+e^- Colliders,” *Phys. Rev. D* **80** (2009) 015003 [[arXiv:0903.3941](#)].
- [41] A. Anastasi *et al.*, “Limit on the production of a low-mass vector boson in $e^+e^- \rightarrow U\gamma$, $U \rightarrow e^+e^-$ with the KLOE experiment,” *Phys. Lett. B* **750** (2015) 633–637 [[arXiv:1509.00740](#)].
- [42] **BaBar** Collaboration, “Search for Invisible Decays of a Dark Photon Produced in e^+e^- Collisions at BaBar,” *Phys. Rev. Lett.* **119** (2017) 131804 [[arXiv:1702.03327](#)].
- [43] **BaBar** Collaboration in 34th International Conference on High Energy Physics. 2008. [[arXiv:0808.0017](#)].
- [44] Z. Liu and Y. Zhang, “Probing millicharge at BESIII via monophoton searches,” *Phys. Rev. D* **99** (2019) 015004 [[arXiv:1808.00983](#)].
- [45] M. Habermehl, M. Berggren, and J. List, “WIMP Dark Matter at the International Linear Collider,” *Phys. Rev. D* **101** (2020) 075053 [[arXiv:2001.03011](#)].
- [46] Y. J. Chae and M. Perelstein, “Dark Matter Search at a Linear Collider: Effective Operator Approach,” *JHEP* **05** (2013) 138 [[arXiv:1211.4008](#)].
- [47] P. S. B. Dev, “Leptophilic Dark Matter at Linear Colliders.” [[arXiv:2111.03024](#)].
- [48] J. Kalinowski, W. Kotlarski, K. Mekala, P. Sopicki, and A. F. Zarnecki, “Sensitivity of future linear e^+e^- colliders to processes of dark matter production with light mediator exchange,” *Eur. Phys. J. C* **81** (2021) 955 [[arXiv:2107.11194](#)].
- [49] B. Barman, S. Bhattacharya, S. Girmohanta, and S. Jahedi, “Catch ’em all: Effective Leptophilic WIMPs at the e^+e^- Collider.” [[arXiv:2109.10936](#)].
- [50] S. Profumo, K. Sigurdson, and L. Ubaldi, “Can we discover multi-component WIMP dark matter?” *JCAP* **12** (2009) 016 [[arXiv:0907.4374](#)].
- [51] Z. Liu, Y.-H. Xu, and Y. Zhang, “Probing dark matter particles at CEPC,” *JHEP* **06** (2019) 009 [[arXiv:1903.12114](#)].
- [52] Q.-F. Xiang, X.-J. Bi, P.-F. Yin, and Z.-H. Yu, “Exploring Fermionic Dark Matter via Higgs Boson Precision Measurements at the Circular Electron Positron Collider,” *Phys. Rev. D* **97** (2018) 055004 [[arXiv:1707.03094](#)].
- [53] A. Birkedal, K. Matchev, and M. Perelstein, “Dark matter at colliders: A Model independent approach,” *Phys. Rev. D* **70** (2004) 077701 [[hep-ph/0403004](#)].
- [54] Z.-H. Yu, X.-J. Bi, Q.-S. Yan, and P.-F. Yin, “Dark matter searches in the mono- Z channel at high energy e^+e^- colliders,” *Phys. Rev. D* **90** (2014) 055010 [[arXiv:1404.6990](#)].
- [55] Y. Hochberg, E. Kuflik, and H. Murayama, “Dark spectroscopy at lepton colliders,” *Phys. Rev. D* **97** (2018) 055030 [[arXiv:1706.05008](#)].
- [56] J. Liu, X.-P. Wang, and F. Yu, “A Tale of Two Portals: Testing Light, Hidden New Physics at Future e^+e^- Colliders,” *JHEP* **06** (2017) 077 [[arXiv:1704.00730](#)].
- [57] I. Alikhanov and E. A. Paschos, “Searching for new light gauge bosons at e^+e^- colliders,” *Phys. Rev. D* **97** (2018) 115004 [[arXiv:1710.10131](#)].

- [58] N. Borodatchenkova, D. Choudhury, and M. Drees, “Probing MeV dark matter at low-energy $e+e-$ colliders,” *Phys. Rev. Lett.* **96** (2006) 141802 [[hep-ph/0510147](#)].
- [59] M. Graham, C. Hearty, and M. Williams, “Searches for dark photons at accelerators.” [arXiv:2104.10280](#).
- [60] Y. Zhang, *et al.*, “Probing invisible decay of dark photon at BESIII and future STCF via monophoton searches,” *Phys. Rev. D* **100** (2019) 115016 [[arXiv:1907.07046](#)].
- [61] **XENON** Collaboration, “Excess electronic recoil events in XENON1T,” *Phys. Rev. D* **102** (2020) 072004 [[arXiv:2006.09721](#)].
- [62] D. Banerjee *et al.*, “Dark matter search in missing energy events with NA64,” *Phys. Rev. Lett.* **123** (2019) 121801 [[arXiv:1906.00176](#)].
- [63] S. N. Gninenko, D. V. Kirpichnikov, M. M. Kirsanov, and N. V. Krasnikov, “The exact tree-level calculation of the dark photon production in high-energy electron scattering at the CERN SPS,” *Phys. Lett. B* **782** (2018) 406–411 [[arXiv:1712.05706](#)].
- [64] S. N. Gninenko, D. V. Kirpichnikov, and N. V. Krasnikov, “Probing millicharged particles with NA64 experiment at CERN,” *Phys. Rev. D* **100** (2019) 035003 [[arXiv:1810.06856](#)].
- [65] X. Chu, J. Pradler, and L. Semmelrock, “Light dark states with electromagnetic form factors,” *Phys. Rev. D* **99** (2019) 015040 [[arXiv:1811.04095](#)].
- [66] A. Berlin, P. deNiverville, A. Ritz, P. Schuster, and N. Toro, “Sub-GeV dark matter production at fixed-target experiments,” *Phys. Rev. D* **102** (2020) 095011 [[arXiv:2003.03379](#)].
- [67] E. J. Williams, “Correlation of certain collision problems with radiation theory,” *Kong. Dan. Vid. Sel. Mat. Fys. Med.* **13N4** (1935) 1–50.
- [68] C. F. von Weizsacker, “Radiation emitted in collisions of very fast electrons,” *Z. Phys.* **88** (1934) 612–625.
- [69] E. Ma and J. Okada, “How Many Neutrinos?” *Phys. Rev. Lett.* **41** (1978) 287. [Erratum: *Phys.Rev.Lett.* 41, 1759 (1978)].
- [70] K. J. F. Gaemers, R. Gastmans, and F. M. Renard, “Neutrino Counting in $e+ e-$ Collisions,” *Phys. Rev. D* **19** (1979) 1605.
- [71] **DELPHI** Collaboration, “Photon events with missing energy in $e+ e-$ collisions at $s^{*(1/2)} = 130\text{-GeV}$ to 209-GeV ,” *Eur. Phys. J. C* **38** (2005) 395–411 [[hep-ex/0406019](#)].
- [72] **SuperCDMS** Collaboration, “First Dark Matter Constraints from a SuperCDMS Single-Charge Sensitive Detector,” *Phys. Rev. Lett.* **121** (2018) 051301 [[arXiv:1804.10697](#)]. [Erratum: *Phys.Rev.Lett.* 122, 069901 (2019)].
- [73] **DAMIC** Collaboration, “Constraints on Light Dark Matter Particles Interacting with Electrons from DAMIC at SNOLAB,” *Phys. Rev. Lett.* **123** (2019) 181802 [[arXiv:1907.12628](#)].
- [74] **SENSEI** Collaboration, “SENSEI: Direct-Detection Results on sub-GeV Dark Matter from a New Skipper-CCD,” *Phys. Rev. Lett.* **125** (2020) 171802 [[arXiv:2004.11378](#)].
- [75] R. Essig, M. Sholapurkar, and T.-T. Yu, “Solar Neutrinos as a Signal and Background in Direct-Detection Experiments Searching for Sub-GeV Dark Matter With Electron Recoils,” *Phys. Rev. D* **97** (2018) 095029 [[arXiv:1801.10159](#)].

- [76] R. Essig, J. Mardon, and T. Volansky, “Direct Detection of Sub-GeV Dark Matter,” *Phys. Rev. D* **85** (2012) 076007 [[arXiv:1108.5383](#)].
- [77] R. Essig, *et al.*, “Direct Detection of sub-GeV Dark Matter with Semiconductor Targets,” *JHEP* **05** (2016) 046 [[arXiv:1509.01598](#)].
- [78] S. Robles, “private communication.”
- [79] M. A. Buen-Abad, R. Essig, D. McKeen, and Y.-M. Zhong, “Cosmological Constraints on Dark Matter Interactions with Ordinary Matter.” [arXiv:2107.12377](#).
- [80] M. Hufnagel, K. Schmidt-Hoberg, and S. Wild, “BBN constraints on MeV-scale dark sectors. Part II. Electromagnetic decays,” *JCAP* **11** (2018) 032 [[arXiv:1808.09324](#)].
- [81] L. Su, W. Wang, L. Wu, J. M. Yang, and B. Zhu, “Atmospheric Dark Matter and Xenon1T Excess,” *Phys. Rev. D* **102** (2020) 115028 [[arXiv:2006.11837](#)].
- [82] Y. Jho, J.-C. Park, S. C. Park, and P.-Y. Tseng, “Leptonic New Force and Cosmic-ray Boosted Dark Matter for the XENON1T Excess,” *Phys. Lett. B* **811** (2020) 135863 [[arXiv:2006.13910](#)].
- [83] Y. Chen, *et al.*, “Sun heated MeV-scale dark matter and the XENON1T electron recoil excess,” *JHEP* **04** (2021) 282 [[arXiv:2006.12447](#)].
- [84] M. Du, J. Liang, Z. Liu, V. Q. Tran, and Y. Xue, “On-shell mediator dark matter models and the Xenon1T excess,” *Chin. Phys. C* **45** (2021) 013114 [[arXiv:2006.11949](#)].
- [85] **BaBar** Collaboration, “Search for a Dark Photon in e^+e^- Collisions at BaBar,” *Phys. Rev. Lett.* **113** (2014) 201801 [[arXiv:1406.2980](#)].
- [86] J. Alwall, *et al.*, “The automated computation of tree-level and next-to-leading order differential cross sections, and their matching to parton shower simulations,” *JHEP* **07** (2014) 079 [[arXiv:1405.0301](#)].
- [87] Y.-S. Liu and G. A. Miller, “Validity of the Weizsäcker-Williams approximation and the analysis of beam dump experiments: Production of an axion, a dark photon, or a new axial-vector boson,” *Phys. Rev. D* **96** (2017) 016004 [[arXiv:1705.01633](#)].
- [88] J. D. Bjorken, R. Essig, P. Schuster, and N. Toro, “New Fixed-Target Experiments to Search for Dark Gauge Forces,” *Phys. Rev. D* **80** (2009) 075018 [[arXiv:0906.0580](#)].
- [89] P. Gondolo and G. Gelmini, “Cosmic abundances of stable particles: Improved analysis,” *Nucl. Phys. B* **360** (1991) 145–179.
- [90] E. W. Kolb and M. S. Turner, [The Early Universe](#), vol. 69. 1990.
- [91] K. Griest and D. Seckel, “Three exceptions in the calculation of relic abundances,” *Phys. Rev. D* **43** (1991) 3191–3203.
- [92] G. Busoni, A. De Simone, T. Jacques, E. Morgante, and A. Riotto, “Making the Most of the Relic Density for Dark Matter Searches at the LHC 14 TeV Run,” *JCAP* **03** (2015) 022 [[arXiv:1410.7409](#)].
- [93] G. Steigman, B. Dasgupta, and J. F. Beacom, “Precise Relic WIMP Abundance and its Impact on Searches for Dark Matter Annihilation,” *Phys. Rev. D* **86** (2012) 023506 [[arXiv:1204.3622](#)].
- [94] I. M. Bloch, *et al.*, “Exploring new physics with O(keV) electron recoils in direct detection experiments,” *JHEP* **01** (2021) 178 [[arXiv:2006.14521](#)].

- [95] E. Clementi, D. Raimondi, and W. P. Reinhardt, “Atomic screening constants from SCF functions. II. Atoms with 37 to 86 electrons,” *The Journal of chemical physics* **47** (1967) 1300–1307.
- [96] A. Pukhov, “CalcHEP 2.3: MSSM, structure functions, event generation, batchs, and generation of matrix elements for other packages.” [hep-ph/0412191](https://arxiv.org/abs/hep-ph/0412191).
- [97] L. Lista, “Statistical Methods for Data Analysis in Particle Physics.”.